ORIGINAL ARTICLE

On the determination of transportation, range and distribution characteristics of Uranium-238, Thorium-232 and Potassium-40: a critical review

Fatih Külahcı[1] · Şerif Çiçek[1,2]

Abstract

This research presents the theoretical and experimental results in real time and suggests spatial models after reviewing the spatial modelling method, which has an important place in earth sciences. It also reveals the geological and geophysical descriptions of mathematical models, calculations and the ease with which one can interpret the results. U-238, Th-232 and K-40 concentrations are determined in water and bottom sediment samples taken from Keban Lake as a sample study area. The point cumulative semi-variogram (PCSV) method application helps to identify the range, distribution and transport of radionuclide at each sampling station. The well-known semi-variogram (SV) is used in many scientific studies. In this study, the SV methodologies are reviewed leading to the application of the PCSV method for the real-time data. The radionuclide distributions in the lake are revealed by means of ten regional models. In addition, iso-radioactivity maps are obtained to provide an overview of the medium radioactivity with characterizations of the transport, range and distribution of the three radionuclides in the lake.

Keywords Spatial modelling · Radionuclide transport in water · Radionuclide range in soil · Behaviours of radionuclides in nature

Introduction

The discovery of radioactivity (Becquerel 1896) brought with it the concept of nuclear energy. Nuclear power plants have been established as a source of nuclear energy, and this type of energy has become available for many years. Some necessary precautions must be taken in using this important energy source. The nuclear accident that took place on April 26, 1986 in the Chernobyl Nuclear Power Plant in Kiev, Ukraine, and the reactor accident that broke out in the Fukushima Dai-Ichi nuclear power plant (FDNPP) on March 11, 2011 are important stops in nuclear reactor accidents. Some of the reactor core of the FDNPP accident was destroyed and radioactive elements such as ^{95}Zr, ^{95}Nb, ^{131}I, ^{132}Te, ^{134}Cs, ^{137}Cs, ^{140}Ba, ^{140}La and ^{90}Sr spread into the atmosphere (Nair et al. 2014).

The past and present nuclear power plant accidents have led many researchers to work on artificial radioactive particles that are spreading from a reactor to the atmosphere and researchers have proposed mathematical models to accurately convey the results of the propagation. These models are based on differential equations systems and include the spatial characteristics of the phenomenon concerned. The first spatial analysis was done by Student (1907), who collected the number of particles per unit area instead of the spatial location of the particles in the liquid. Later, Fisher (1936) used spatial analysis in agriculture. Yates (1939) examined the effect of correlation on spatial analysis. The spatial analysis helps to quantify the groundwater quality behaviour (Bhuiyan et al. 2016; Kavurmaci 2016). In addition, irrigation and groundwater quality parameters were also determined by means of the same approach (Arslan

✉ Fatih Külahcı
  fatihkulahci@firat.edu.tr

[1] Nuclear Physics Division, Physics Department, Science Faculty, Firat University, 23119 Elazig, Turkey

[2] Kemalpasa Neighborhood, Istanbul Arel University, Halkali Street No: 101, Sefaköy, Küçükçekmece, 34295 Istanbul, Turkey

2017). On the other hand, spatial analysis was also used for soil quality identifications (Some'e et al. 2011).

The techniques of spatial analysis and spatial modelling are based on "variance" and "covariance" concepts, which are valid provided that regularly located sampling points and variable records are available. Unfortunately, in most of the cases the data are often inadequate for the implementation of these techniques. To take into consideration such deficiencies, an effective method was suggested by Matheron (1963) through the "semi-variogram" concept. The semi-variogram (SV) is defined as the sum of consecutive half-square differences and is ordered by an increasing scale at selected distances from all possible pairs of sample points in a region (Şen 1989). The methodological progress of SV gained a different perspective with the cumulative semi-variogram (CSV) method based on the cumulative sum of the half-square differences of data (Şen 1989). Later, Şen (1998b) proposed a point cumulative semi-variogram (PCSV) method, which proposes independent models for each station and characterizes the transport, range, physical, geophysical and chemical properties of the variables in these stations along many directions. This method is particularly useful if the sampling points are scattered irregularly within the study area, which is often the case in practical applications (Şen 1998a). The trigonometric PCSV is proposed, which can detect the behaviour of the variables depending on the trigonometric parameters (Şahin and Şen 2004). Estimation and temporal changes in spatial variations were also considered through the absolute PCSV (Külahcı and Şen 2009a) and spatiotemporal PCSV (Külahcı and Şen 2009b) methods. The PCSV method and its derivatives have been used by many researchers in different fields. It has been successfully applied for spatial modifications of radionuclides (Külahcı and Şen 2007, 2009b).

Natural radioactivity

At the top of the elements that form natural radioactivity are uranium and thorium. These two radioisotopes have two different series of decays. The series end with decay in the stable lead isotope. The nuclei emit alpha, beta, gamma and neutrinos as a result of degradation. Natural uranium has three radioisotopes: ^{234}U, ^{235}U and ^{238}U. In general, 99.27% of natural uranium constitutes ^{238}U. Another element that generates natural radioactivity is thorium with its six radioisotopes in the three decay series, which are ^{234}Th, ^{232}Th, ^{231}Th, ^{230}Th, ^{228}Th and ^{227}Th. Thorium is less active than uranium in structure (Cowart and Burnett 1994). U and Th are large sized (Kenny et al. 2019; Rehman et al. 2013) and behave differently in nature and are not chemically compatible with most minerals (Gascoyne et al. 1982; Petrus et al. 2016). Under these conditions, they tend to form in

the alkaline rocks (da Costa et al. 2016; Ivanovich and Harmon 1982) and exhibit similar behaviours. The ratio between them is 3/4 (Th/U) (Wu et al. 2016). The concentrations of these elements tend to increase in silica (Batuk et al. 2013). Granites have the highest U and Th content (Banks et al. 1995). Even though the silica ratio in the granite (Verma et al. 2003) is relatively higher, the amount of U rarely exceeds 30 ppm, and if the silica ratio is low, the amount of U is 0.1 ppm or less (Rogers et al. 1969).

Degradation series radionuclides tend to accumulate under certain environmental conditions, in particular terra rossa type on limestone (Halicz et al. 2008; Yalcin and Ilhan 2013). This kind of soil leads to a very strong disequilibrium in the U series radionuclides. In terra rossa type of soils, primordial radionuclides, which constitute 95% of the external gamma dose rate, are trapped and constitute the storage of important radionuclides. The main contributions to these warehouses are from 35% ^{40}K, 50% ^{232}Th series and 15% ^{238}U series (Laubenstein and Magaldi 2008).

Radioactivity in the soil is mainly due to weathering sedimentation, leaching/sorption and precipitation processes of rocks. High U activity in the soil is associated with soil organic matter (Hansen and Huntington 1969; Talibudeen et al. 1978). (Hansen and Huntington) reported in 1969 that the high organic matter content of the soil had the accumulation of Th. Because organic substances are strongly complexed with tetravalent Th, the mobility of Th in the soil increases. In addition, alluvial soils are the structures that will cause the large mobility of Th as organic complexes. Th has a higher concentration in alluvial soils and its distribution is more homogeneous (Hansen and Stout 1968; Valkovic 2000). U and Th are usually found in the soil in the valences of +VI and +IV, respectively (Li et al. 2018a).

Formation of natural radioactivity in lake environment

Rivers can carry radionuclide-containing soils to long distances. Atmospheric factors also allow the radionuclides to rise to the surface. Closed seas and estuaries form clay and organic materials, which can turn into an artificial obstacle for radionuclide transport, making it difficult to transport uranium in such environments, because uranium is absorbed by organisms and clay and some clay layers cover very large areas. For example, America has an average of 79 ppm uranium, with a world average of 2 ppm (Valkovic 2000). U, transported to the environment of clay and organic matter, is reduced to +4 immobile and absorbed by organic or clay structures (Rodriguez et al. 2017). In America and Australia, sandstones near the lakes contain economically significant amounts of uranium. Uranium-bearing waters, if flowing along sandstones, are absorbed by sandstones and retaining elements, and a precipitate forms on the sand. Formations

such as erosion cause the soil on the surface to change location. Uranium in the lake or river can be transported to other lakes and rivers, partly due to erosion. Due to environmental conditions, elements such as uranium can be oxidized and oxidized uranium in water has transportability. Uranium in surface waters is released and transported from the surface and in this way the number of uranium nuclei increases. On the other hand, the sediments contribute to the accumulation of radioactivity after the natural processes before they harden. Erosion-resistant minerals can be said to have higher radioactivity compared to these minerals. As an example, sand in north-east Florida is rich in monazite and contains significant amounts of thorium. The radioactive enrichment that occurs due to the high attraction properties of monazites can be transported along the shores. Thus, water contains natural radioactivity in small and variable quantities from thorium, uranium and their decay series products and potassium (L'Annunziata 2003; van der Loeff and Moore 2007).

Volcanic formations cause a large amount of particulate matter in the environment. These particles emit atmospheric sources of natural radioactivity that they absorb in the lower layer of the ground surface. The particles that accumulate in the atmosphere descend into the earth with natural phenomena such as precipitation and winds. Sometimes, they can be transported to the lake, sea or ocean as a result of natural phenomena (Ferronsky 2015). Water is an important transport tool for uranium and decay series elements (Tricca et al. 2001). River waters and sediment materials poured into the sea carry radioactive elements. The range of dissolved uranium concentrations in rivers is 4.8×10^{-3}–8.3×10^{-5} Bq/l (becquerel/litre) and the uranium concentration in ocean waters is 0.04 Bq/l. Thorium is found in rivers and oceans at very low levels, but it is deposited on the sea and lake floor by the transport by the rivers (Not et al. 2012). Groundwater can be found in a wide range of different concentrations with an appropriate environment for the separation of radioactive particles (Tudorache and Marin 2012). For example, uranium was measured at different concentrations from 1 up to 100 ppm. In contrast, all thorium isotopes are generally low in water (Ojovan et al. 2005).

Potassium-40

There are 28 isotopes of potassium, of which only three are natural (^{39}K, ^{40}K, ^{41}K) and only ^{40}K is radioactive (Atwood 2013). Through volcanic emissions, the radioisotopes, K, Pb, Bi, Po, and Rn, are emitted into the atmosphere.

Potassium can be taken by means of plant roots, mainly through two mechanisms, which are ion channels and specific carriers. K^+ is also effective in the reception of radioactive Cs. High soil concentrations prevent Cs uptake (Atwood 2013; Ciuffo and Belli 2006); therefore, there is a strong correlation between these two radionuclide concentrations in the opposite direction.

Generally, the ^{40}K is in mineral form and is a component of various rocks and dusts, so that it can accumulate in soils and minerals and as a soluble electrode in water. This radioactive isotope has an interesting distortion history and has a very long half-life of 1.248×10^9 years. It can be disintegrated by three different beta radiations. With a probability of 89.2%, it is decayed to ^{40}Ca by emitting a beta particle (electron) with a maximum energy of 1.35 MeV. On the other hand, with a probability of 10.72%, the maximum energy is disintegrated to ^{40}Ar by making a gamma structure with 1.463 MeV. Finally, with a very low likelihood, it is decayed to ^{40}Ar by making a positron emission with a probability of 0.001%. Potassium is the most important source of natural activity in humans and animals. A human body has about 160 g of potassium. In contrast, ^{40}K has an abundance of 117×10^{-6}. From this, it can be calculated that 0.0187 g is ^{40}K (Engelkemeir et al. 1962; Samat et al. 1997). Kiss et al. (1988) reported that ^{40}K, ^{214}Bi and ^{208}Tl activities decrease with the increase in clay content in the soil. The ^{214}Bi and ^{208}Tl are the daughter nuclei of ^{238}U and ^{232}Th, respectively.

The average amount of radiation caused by ^{40}K is 0.30 mSv year^{-1} (effective dose equivalent) (Valkovic 2000). In modern power plants, a relatively small portion of radio nuclei is carried by fly ash through flue gases: ^{40}K: 500 Bq kg^{-1}, ^{238}U: 200 Bq kg^{-1} and ^{232}Th: 200 Bq kg^{-1}. Using these values, the amounts of atmospheric oscillations can be estimated as ^{238}U: 1500 MBq GW^{-1} year^{-1}, and ^{232}Th: 1500 MBq GW^{-1} year^{-1} (Papastefanou 2010; Suhana and Rashid 2016; Valkovic 2000).

Along with the phosphate fertilizers are used in agriculture including radioactive metals such as uranium, thorium, radium and potassium enter the environment. Radioactive pollutants are an important research topic (Nwankpa 2017).

Thorium-232

Thorium, an element of the uranium decay chain, has an atomic number of 90 and atomic weight of 232.038 g/mol. It is abundant in river and ocean waters and can be transported by rivers and accumulated in sea and lake sediments. Thorium exists in low concentrations in regions where gold is normally present. Thorium's presence can be detected by the presence of thoron gas, which comes out of the gold mines and interferes with the atmosphere. In some areas, thorium has high concentrations of black sand layers on gold bed reefs (Buccianti et al. 2009; World Nuclear Association 2013).

Thorium is an element with low geochemical mobility. Like U^{+4}, Th^{+4} is also relatively immobilized, because the cation-exchange resins are adsorbed above. Thorium forms metal complexes with citric acid, oxalic acid and acetyl

acetone (Sheppard 1980). It is found in nature as tetravalent ions. Th is not oxidized to a similar form of uranyl ion, i.e. a hexavalent state under geological conditions (Adams et al. 1959; Edahbi et al. 2018; Li et al. 2019; Morales-Arredondo et al. 2018).

In the solution, Th precipitates as a hydrolysate because of the very high ionic potential of the tetravalent ion and is rapidly adsorbed. Like U, Th is also found in high amounts in minerals such as zircon, monazite and xenotime (Horie et al. 2010; Mesbah et al. 2016). It forms a compound with water and can easily adhere and collapse on surfaces. Th is added to the particles to receive the form of radiocolloids and can be transported in this way (Sheppard 1980).

Th does not crystallize in basic magmatic structures. One can see that it is richer in silicic magma structures such as granite. It may occur in the simple isomorphic structure of tetravalent zirconium and may occur as isomorphic thorite ($ThSiO_4$) (Bingen et al. 1996). The transport of Th in solutions is in very minor amounts, and therefore it can be called immobile. It can usually be transported in significant amounts through wind and water erosion by adhering to clay particles and then deposited in the soil system (Braun and Pagel 1994; Ndjigui et al. 2008).

Thorium decay chain

^{232}Th is the initial isotope of the thorium decay chain and it occurs effectively throughout natural thorium. In other isotopes, uranium and thorium are associated with a small amount in relation to short-lived decomposition products. ^{232}Th is decayed by alpha emission and has a half-life of 1.405×10^{10} years. This value is three times bigger than the world's age. The thorium decay chain ends with a decomposition of ^{208}Pb. ^{228}Ra and ^{228}Th have 5.75 years and 1.91 years half-life, respectively, and the half-life of all other isotopes is less than 5 days. ^{232}Th is a productive element, which absorbs the neutrons and by this means becomes a divisible isotope, ^{233}U (Crossland 2012).

Elements of the ^{232}Th decay chain occur with alpha emission or gamma emission at low levels. As an exception, ^{212}Bi is formed by significant amount of beta and gamma emission. ^{212}Bi has larger and higher maximum energies than the energy range of the uranium decay chain (3.95–8.78 MeV). The major beta emitters in the thorium chain are ^{228}Ra, ^{228}Ac, ^{212}Pb, ^{212}Bi and ^{208}Tl. Much of the gamma emission formed in the ^{232}Th chain is in the ^{224}Ra decay section. More than 95% of the gamma emission in the chain is in this lower decay chain. The dominant gamma radiation in the chain is ^{208}Tl. The emission has an energy range of 0.511–2.614 MeV. Due to the abundance of ^{208}Tl and high energy, it generates strong gamma fields in any material that is extensively present (Bonotto 2014; Charro and Pardo 2014; Jamison 2014; Middleton et al. 2014; Shmelev et al. 2014).

Uranium-238

Uranium may have an extremely high level of mobility, if the calcium salts in the environment have low concentrations and U may be concentrated in water in suitable geochemical environments. U, which has existed since the beginning of the world, is found in new forms of rocks formed by natural disintegration. If these rocks are not fragmented, uranium eventually reaches secular equilibrium (Deschamps et al. 2004; Vigier et al. 2005). Adams et al. (1959) report that igneous rocks contain U ranging from 0.001 mg/g to 30 mg/g. These concentrations increase with increasing acidity (Sheppard 1980). The amount of U in the metamorphic rocks ranges from 0.11 mg/g to 57 mg/g and is about 7 mg/g. The sedimentary rocks have between 0.1 and 245 mg/g (Kacmaz and Burns 2017; Masod Abdulqader et al. 2018; Sheppard 1980). Uranium can be absorbed by water in loose soils through plants and absorbed by their roots (Serre et al. 2019). Therefore, analysis of the soil surface is important for the determination of the amount of U in the soil.

Since ^{234}U is subjected to more than ^{238}U leaching processes in rock erosion, using the ^{234}U/^{238}U ratio to determine wear rates does not yield healthy results (Hansen and Stout 1968). This situation, i.e. the formation of more than ^{238}U of the ^{234}U in the upper layers of the soil, inhibits the capillary movements of the plants (Hansen and Stout 1968; Serre et al. 2019).

Uranium forms increase their solubility in an oxygenated environment (Latta et al. 2016). The radius of uranium ions is large, it can be absorbed by clay and some other lattice minerals (Sheppard 1980); therefore, U in the shales may form as adsorbed ions.

Uranium is an element that can be found everywhere with appearance, silver color, bright and quantity change. ^{238}U, an isotope of uranium, is a radioactive element with an atomic number of 92 and an atomic weight of 238.0289 mol. It is included in the actinide series in the periodic table. The metallic uranium has a density of 19 g/cm^3 (WHO 2018). According to researches, in the early periods of the world about 10^9 years ago, uranium oxide particles could be carried over long distances through rivers. It is thought that gold was deposited in these river basins during these periods. The uranium oxide particles carried along the rivers were separated from the less dense substances and stored in river basins. These natural reservoirs were deeply buried in natural conditions and metamorphosed as quartz pebble conglomerate deposits, which are important uranium storages (Chakrabarti et al. 2011).

The main contribution to gamma dose ratios is 99% from the ^{238}U degradation series (^{214}Pb and ^{214}Bi). The dose rates

are spread over 30 cm from the top of the soil. The dose rates depend on the geology of a research area, the diversity of rocks and the variety of radionuclides of the soil. The highest dose rates are usually found in igneous rocks. This situation depends on the amount of silicate formations in igneous rocks. Excessive silicate structures result in high gamma dose ratios (Chan et al. 2007).

Uranium decay chain

U, which differs from igneous, metamorphic or sedimentary rocks, is generally distributed in the form of U^{+2} or one of its complexes (Meinhold 2010). Uranium re-accumulation is facilitated indirectly by reduction reactions through processes produced by living organisms and enriched in sedimentary rocks and similar structures. As a result of hydrological and atmospheric events, the accumulations of U begin to move towards or near the earth (Braun et al. 2017).

There are three isotopes, natural uranium, ^{234}U, ^{235}U and ^{238}U, with half-lives as long as 244,500 years, 703.8 million years, and 4.468×10^9 years, respectively (WHO 2018). ^{238}U is the one with the highest rate of abundance from natural uranium isotopes and it can catch slow neutrons and then decays to ^{239}Pu by making 2 beta emissions with splitting by fast neutrons. However, if one or more new generations of nuclei have a fast fission, they do not contribute to the chain reactions due to the energy loss in the inelastic scattering it generates with the neutron. Natural uranium contains ^{238}U at around 99.284% and its half-life is 4.468×10^9 years. Depleted uranium has ^{238}U at its highest concentration. To decompose the uranium chain into a stable lead, 11 different decay steps are needed. During decay, each radionuclide radiates a characteristic radiation. Characteristic energies and propagation probabilities cause the spread of alpha particles, beta particles, and gamma photons. The emission may contain a mixture of energy or energies (Scott 1982; Valkovic 2000).

A large majority of uranium decay chain elements have short half-lives. There are only five radionuclides, whose half-lives are more than 1 year, which are ^{238}U, ^{234}U, ^{230}Th, ^{226}Ra and ^{210}Pb. The half-life interval of these elements is 22.3 and 4.5×10^9 years. The remaining radionuclides are ^{222}Rn, ^{210}Bi, and ^{210}Po with their half-lives from 3.82 to 182 days. First, there are eight radionuclides that begin to degrade through alpha propagation, which are ^{238}U, ^{234}U, ^{230}Th, ^{226}Ra, ^{222}Rn, ^{218}Po, ^{214}Po and ^{210}Po. These decays occur either only with alpha emission or with gamma photon matching in very small quantities. The characteristic energy of each alpha particle emitted is between 4.2 and 7.69 MeV for the above radionuclides. Alpha particles have a limited range in the air (4 MeV at 2.5 cm and 7 MeV at 6 cm). Alpha-emitting radionuclides can emit alpha in only one energy (Hernandez et al. 2005), for example, Rn

is 5.49 MeV, Po is 6.00 MeV, and Po is 7.69 MeV; or each of them can emit alpha particles with different energies and in different probabilities (Saleh and Abu Shayeb 2014), e.g. ^{234}U: 4.72 MeV (28%) and 4.77 MeV (72%), ^{226}Ra: 4.78 (95%) and 4.6 MeV (6%). The above alpha emitters have five long half-life alpha emitters that cause radiological hazards (Frybort 2014; War et al. 2012; Watford and Wethington 1981), which are ^{238}U, ^{234}U, ^{230}Th, ^{226}Ra, and ^{210}Po. Additionally, radon and three short-lived alpha-emitting are ^{222}Rn, ^{218}Po, ^{214}Po. They have low activity; they do not present a radiological hazard. ^{210}Po is a very fast decaying alpha emitter. On the other hand, there are six radionuclides generated by beta decay such as ^{234}U, ^{234m}Pa, ^{214}Pb, ^{214}Bi, ^{210}Pb, ^{210}Bi (Attendorn and Bowen 2012; Ivanovich and Harmon 1992; Valkovic 2000).

When alpha and beta decays are present, gamma radiation is also common. If the energy of the alpha emission is relatively low, it can be said that the alpha emitters are not related to the gamma emission. For example, a ^{226}Ra alpha emitter emits a low-energy gamma photon of 0.186 MeV. Gamma abundance percentages are generally low, and therefore do not cause much harm to the environment. Almost all of the gamma propagation that occurs in the uranium chain is from the lower series of chains and especially from ^{214}Bi. The abundance of emissions is highly effective at energy range of 0.2–2.5 MeV. Compared to decay products and ^{226}Ra, radium is a very weak beta emitter. Thus, ^{226}Ra's short half-life nuclide products trapped in soil and similar materials are an important emitter of the gamma dose. For this reason, the higher concentration of radium per gram and the greater amount of material in a region lead to a more intense gamma radiation (Kaufman 2005).

Experimental

Determination of radioactivity levels

The water and bottom sediments are taken from the surface of the Keban Dam Lake (30 cm depth) and from the bottom of the lake using Nansen tube and bottom bucket. Water samples are in 0.1 l volume. Acidic water samples are reduced to two acid levels and allowed to remain stable until the time of measurement. Evaporation is then carried out at 60 °C without boiling. The sediments in the beads are transferred to planchettes with pure water and dried under UV lamp. Sediment samples are collected and transported to laboratory in closed containers. The samples of the lake sediment are also transferred to the planchettes, which had been dried in an oven and weighed again, and their net weights calculated. So, sediment samples are also prepared for measurement.

Several mathematical operations are required to determine the activity levels. First, the net count value is determined in units/s. The mathematical expression for the net count value is as follows.

$$C = \frac{N}{t_N} - \frac{BG}{t_{BG}}, \tag{1}$$

where N is the count number, BG is the background count, t_N is the counting time and t_{BG} is the count time for the base level. After the net count is reached, the activity level is calculated as

$$A = \frac{C}{M_N P_\gamma \varepsilon}, \tag{2}$$

where M_N is the sample weight, P_γ the gamma ray emission probability, and ε the device efficiency. The gamma energies used in the ^{238}U, ^{232}Th and ^{40}K measurements are given in Table 1. The standard deviations of the measurements are approximately 10%. Gamma spectroscopic system with 2-in. $\times$ 2-in. Na(Tl) well-type detector is used in the measurements. The measurement method, the calibration of the devices and the calculation of the detector efficiencies are made as mentioned by Külahcı (2016a, b).

Spatial modelling

A regional variable (ReV), a concept that has been included in earth sciences, is a term having random regional variability and different characteristics. The identification of the regional variable and the detailed examination are of great importance in terms of its characterization. Studies on earth sciences have shown that spatial dependence plays an important role in characterizing regional change (Cressie 1988).

Variance and covariance techniques, which have an important place in the literature of earth sciences, are not sufficient to explain directly regional dependence. For this reason, the SV technique developed by Matheron (1963) has been used by many researchers in different fields, such as geology, mining, hydrology and earthquake prediction, to characterize spatial diversity (Carr et al. 1985; Clark 1979b; Genge et al. 2017; Göl et al. 2017; Journel 1986; Lütkepohl and Krätzig 2004; Oldham et al. 2017; Rosemary et al. 2017; Zakirov et al. 2017).

Table 1 Gamma and beta energies of radionuclides

Radionuclide	Radiation type	Energy (MeV)	Probability (%)
^{238}U	Beta	0.06329 (^{234}Th)	0.038116
^{232}Th	Gamma	0.338 (^{228}Ac)	0.11357
^{40}K	Gamma	1.463	0.1067

Semi-variogram methodology

Variable values obtained from predetermined sampling stations in the study area are influenced by each other. For this reason, they vary depending on the distance between them. As the distance between stations increases, this change decreases. The SV function has been used by different researchers (Journel 1986; Matheron 1970; Velasco-Forero et al. 2009). SV can be defined as the sum of consecutive semi-square differences (Antoine et al. 2009; Dai et al. 2005; David 2012; Goovaerts 2008; Valeriano et al. 2006).

The SV function requires uniformly distributed sample points. Due to the geological structure and environmental conditions of the study area, the sampling stations may not be uniformly distributed. This is a problem in the SV calculations (Clark 1979a). The SV is calculated as the average of the difference between all pairs possible. Increasing the distance between two points causes the variance values to be different, which means that the variance increases. The variance can be defined as the interval in which a variable varies. After the variogram operations, a two-dimensional scatter graphic is obtained, which is matched with an appropriate theoretical mathematical model (Deutsch and Pfeifer 1981; Journel 1986).

In general, the results obtained in each study may not have a non-regular structure and cannot be expressed mathematically. The modelling is pre-programmed and efforts are made to estimate the regional behaviour of the variable. The mathematical expression of this function can be expressed by the following expression.

$$\gamma(h) = \frac{1}{2N} \sum_{i=1}^{N_d} \left(Z_i - Z_{i+d} \right), \tag{3}$$

where $\gamma(h)$ is the SV value at the distance h, Z_i is the value of the regional variable i, Z_{i+d} is the value of the regional variable measured after the distance d from i and N_d is the total number of sample distances (Clark and Eng 2001). As noted earlier, the SV requires regularly distributed sampling stations. The difficulties that this requirement brings have been explained by Şen (1989).

After the cumulative SV (CSV) (Şen 1989) and point cumulative SV (PCSV) (Şen 1998b) methods in the historical development of semi-variogram (SV), trigonometric PCSV (TPCSV) (Şahin and Şen 2004) has resolved angular deficiencies of SV and subsequent spatial analysis methods. After TPCSV, absolute PCSV (APCSV) was recommended. The classical solid/liquid distribution coefficient (K_d) between APCSV, water–sediment, water–air and or sediment–air systems eliminates the deficiencies of K_d. APCSV calculates distributions between chemical and physical variables by considering all sampling stations. Thus, it achieves more realistic results than conventional K_d. After APCSV,

_ENREF_72 proposed the SpatioTemporal PCSV, which is capable of modelling both spatial and temporal changes to eliminate the temporal effects of SV.

Semi-variogram parameters

The SV has basically three parameters: the nugget effect, sill and radius of influence as shown in Fig. 1. Each parameter has a different meaning and provides useful information about the characteristics of the relevant variables and variables.

Nugget effect The nugget effect can be said to be the mathematical expression of the change resulting from the physical nature of the measured variable. It reflects the difference between the samples that are very close to each other, but not exactly in the same position. In a variogram graph, the positive intersection over the y-axis at $h = 0$ is called the nugget effect and is represented by the C_0 parameter (Carrasco 2010; Clark 2010; Glikson 2007; Isaaks and Srivastava 1989a).

When the independent variable is related to the distance, there is a limit value determined from the data, which is the distance between two points closest to each other at the sample points. It is not possible to notice the change in the working distance at a lower distance than this value. This causes discontinuity in the variogram and also in the regionalized variable and this limit value is called nugget effect, which indicates that an error or sudden variable variation exists. The graphical representation of the nugget effect is shown in Fig. 1 (Birol and Saridede 2013; Dauphas and Pourmand 2015; Isaaks and Srivastava 1989a). The nugget effect indicates the discontinuity of the SV from its origin (Clark 1979c; Isaaks and Srivastava 1989a).

Sill If the regional variable is rich in ore content and later in the form of a poor transition, the variogram stops incrementing after a certain distance and remains constant at a certain value. This value, which the increase of variogram stops, is called sill, and it is also the point where the variogram function reaches the turning point. Sill formation is evident in Fig. 1 (Haug et al. 2018; Journel and Huijbregts 1978; Rabbel et al. 2018; Vandyk et al. 2018; Yao et al. 2018).

Radius of influence It is defined as the distance at which the variogram reaches the sill value. After this distance covariance is zero, which means that the data are no longer related to each other. A point that is left in this area affects the values of other points in the area. The radius of influence means that the event of interest is not stationary and the variance

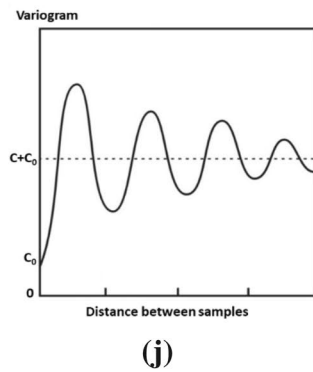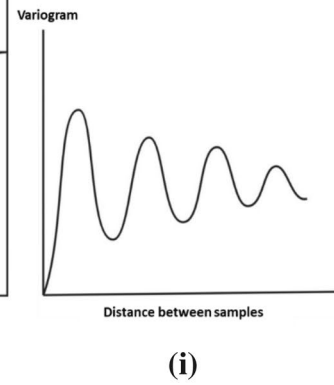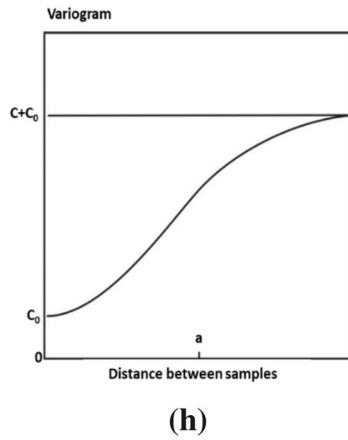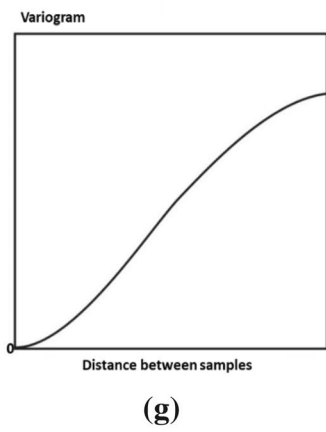**Fig. 1** Representation of variogram parameters by the variogram model
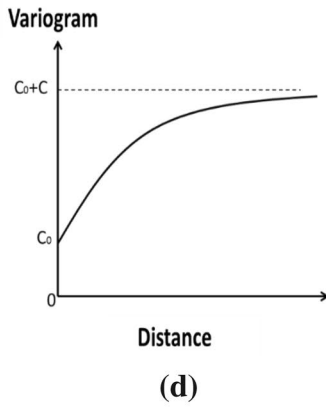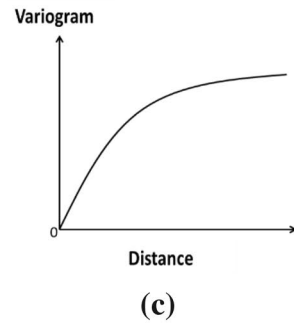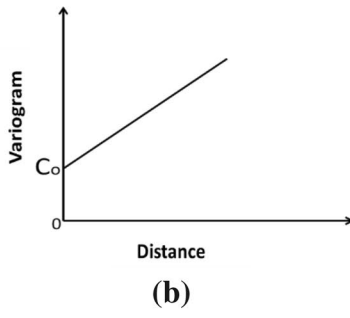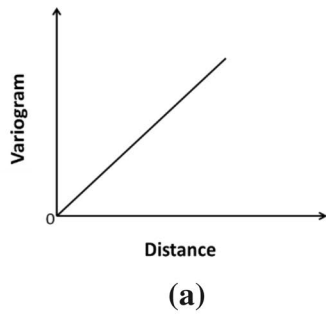
(a)

(b)

(c)

(d)

(e)

(f)

(g)

(h)

(i)

(j)
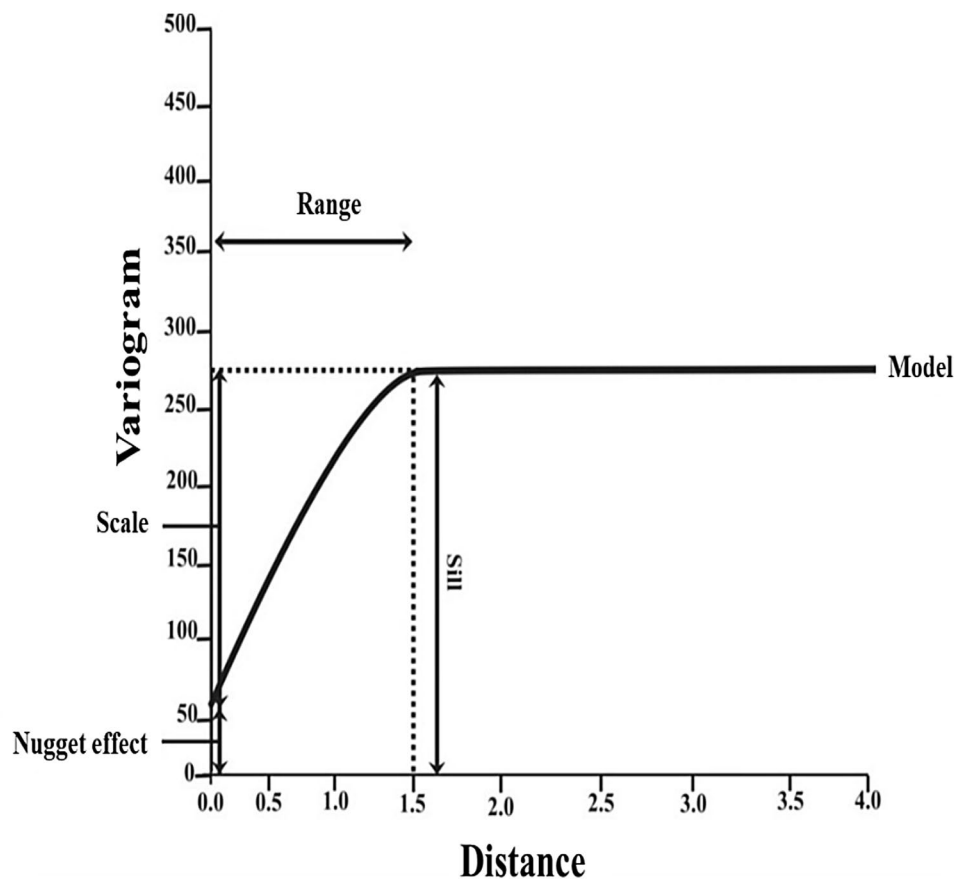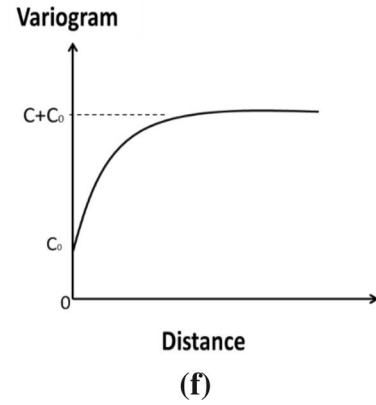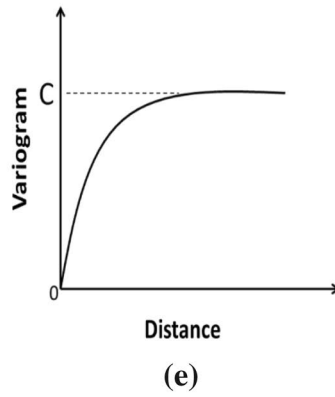
◀**Fig. 2** a Linear variogram model without nugget effect, **b** linear variogram model with nugget effect, **c** exponential model without nugget effect, **d** exponential model with nugget effect, **e** spherical model without nugget effect, **f** spherical model with nugget effect, **g** Gaussian model without nugget effect, **h** Gaussian model with nugget effect, **i** hole-effect model without nugget effect, **f** hole-effect model with nugget effect

goes to infinity, but on the other hand there is no covariance. In such cases, sill and radius of influence do not make any sense (Khosravi et al. 2018; Özyavuz et al. 2015; Varouchakis et al. 2016; Verworn and Haberlandt 2011; Zhang et al. 2018). The representation of these variables in a variogram model is given in Fig. 1.

Major models in the semi-variogram

The variogram must be known at all distances in determining the properties of the regional variable, and in particular in estimating the values at the unmeasured points. This requires modelling the variogram, i.e. adapting a function to the variogram values.

There are many variogram models. Today's variogram models are generally divided into two groups according to whether they have a peak value or not:

1. Peak models.
2. Models without peaks.

Peak models are globally in the form of exponential and Gauss model types. For non-peak models, the linear model can be given as an example (Journel and Huijbregts 1978).

Journel and Huijbregts (1978) classified the frequently used theoretical models as follows:

Models (or transition models) with a sill and a linear behaviour at the origin:

(a) spherical model,
(b) exponential model, and a parabolic behaviour at the origin,
(c) Gaussian model.

"Model without a sill" (the corresponding random function is then only intrinsic and has neither covariance nor finite a priori variance):

(a) models in $|h|^\theta$, $\theta \in]0, 2[$,
(b) logarithmic model.

Linear model This is the simplest model of the variogram, where it is proportional to the distance of the variable. This model has a positive intersection on the variogram axis if it has a nugget effect and has always a mode that varies proportionally with the distance to the positive gradient slope. The

linear model shows that the event has regional dependence and that the event develops in accordance with an independent process (Hohn 1999). Thus, in the objective analysis of such an event, only the average and standard deviation need to be known. In the case, where the linear model does not have a nugget effect, the model graph is as shown in Fig. 2a. If a linear model has a nugget effect, the model graph is as shown in Fig. 2b and the formula is given in Eq. 4:

$$\gamma(h) = C_0 + ph, \tag{4}$$

where γ is the variogram between the two points concerned and h represents the value corresponding to the distance, p indicates the slope of the curve and, finally, C_0 indicates the influence of the nugget on the variogram axis. The linear model does not have a sill effect, because it does not have a horizontal state (Journel and Huijbregts 1978; Şen 2009). Unknown C_0 and p parameters can be solved with the help of a sample SV (Şen 2009).

Exponential model The variogram drawn for this model has a curvature form and approximates the sill asymptotically. It is based on an important parameter such as the sill and approaches asymptotically as far as the range. If this model does not have a nugget effect, the graph will be as in Fig. 2c. If the model has a nugget effect, the graph is as shown in Fig. 2d and is given by Eq. 5:

$$\gamma(h) = C_0 \left[1 - \exp\left(-\frac{h}{a} \right) \right] \quad h > 0, \tag{5}$$

where γ is the variogram value and h refers to the distance between the two points concerned. Furthermore, C_0 and h are model parameters (Clark 1977a), where C_0 is the nugget effect (Chen and Gong 2004; Clark 1979b; Journel and Huijbregts 1978). If $h = a$, the exponential model reaches a sill, which is clearly visible in Fig. 3.

Spherical model This model was recommended first by Matheron (1963) and is the most widely used in variogram modelling depending on two parameters, the radius of the effect and the sill value that indicates the range of the particle in the graph. Otherwise, the variogram axis (*y*-axis) may also have a positive intersection, called the nugget effect. The graph with no nugget effect is shown in Fig. 2e. The graph in Fig. 2f has a nugget effect. The equations for this model are expressed by Eqs. 6 and 7 (Isaaks and Srivastava 1989b):

$$\gamma(h) = C_0 + C \left[\frac{3h}{2a} - \frac{1}{2} \left(\frac{h}{a} \right)^3 \right] \quad 0 < h < a, \tag{6}$$

$$\gamma(h) = C_0 + C \quad h = a, \tag{7}$$

where γ is the variogram value, h the distance between the two points concerned and a the parameter expressing
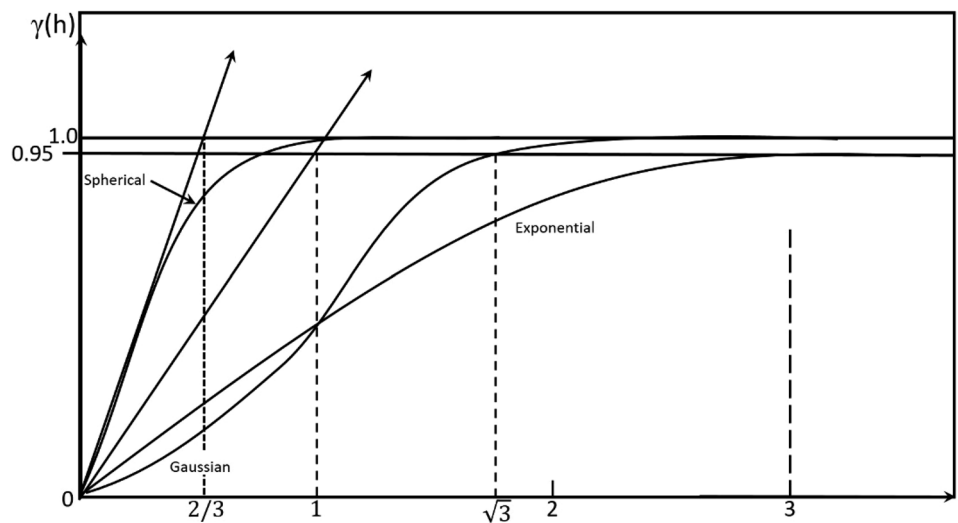
the radius of the influence of the variogram. The spherical model increases with increase in distance h starting from the origin. When the radius of influence is reached, the increase stops and at this distance the value of the variogram reaches the highest value (Fu et al. 2018; Oropeza et al. 2018; Pingguo et al. 2016; Xu et al. 2000).

The difference between the spherical and exponential models is the distance at which their tangents at the origin intersect the sill as in Fig. 3, where $h = 2a/3$ is two-thirds of the range for $h = a = a'/3'$ and one-third of the practical range for the exponential model (Journel and Huijbregts 1978).

Gaussian model This model refers to events that are similar in extreme continuous or short distances. The relationship is strong at close distances and weak at distances. It is the only variogram model with parabolic behaviour at the origin. As the distance increases, the threshold value reaches an asymptotic value and is generally recommended in the form of $a' = a\sqrt{3}$, with range $\gamma(a') = 0.95 \approx 1$ (see Fig. 3). The model has a drift effect at $r < 2a/3$ distances. This effect prevents the Gaussian model from being mixed with parabolic behaviour at great distances. At small distances, $h < 2a/3$, the model (Gaussian) can either be interpreted as a drift effect or as a stationary Gaussian structure (Zhang et al. 2008). It implies that the continuity and uniformity of the regional variable over short distances are rare (Ersoy and Yünsel 2018; Gundogdu and Guney 2007; Valeriano et al. 2006). If the model does not have the nugget effect, the graph is as shown in Fig. 2g (Isaaks and Srivastava 1989b). The model with the nugget effect is as in Fig. 2h and the mathematical expression of this model is given by Eq. 8:

$$\gamma(h) = C_0 \left[1 - \exp\left(-\frac{h^2}{a^2} \right) \right] \quad h > 0, \tag{8}$$

where γ is the variogram value, h is the distance between points of interest and C_0 is the nugget effect. These models can have a sill.

Models without a sill as in r^θ are also available. The models range $\gamma(r) = r^\theta$ with $\theta \in]0, 2[$. The change is given in Fig. 4.

As the θ value increases, the behaviour of $\gamma(h) = h^\theta$ in the origin is more uniform and increasingly corresponds to regular spatial variability. Models for $\theta \in]1, 2[$ are indiscernible from a parabolic drift effect. Similarly, the logarithmic model $\gamma(h) = \log h$ also has no sill.

Hole (wave) effect model It is a model developed to express cyclic or periodic relation between two samples. It is based on two important parameters: the cyclic distance (the entire period of periodicity) and the sill around the fluctuation. In
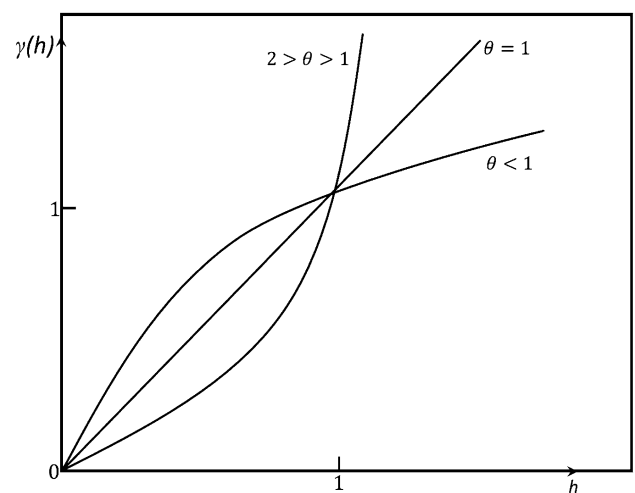

Fig. 4 Models in r^θ (modified from Journel and Huijbregts 1978)

addition to these, it may also have a nugget effect as in other model types (Cowan and Cooper 2003). In the case of not having the nugget effect, the model graph is shown in Fig. 2i. In the case of the nugget effect, the model graph is given in Fig. 2i and its equation is expressed by Eq. 9:

$$\gamma(h) = C + C_0^2 \left[1 - \left(\frac{\sin\left(\frac{\pi h}{a_0}\right)}{\left(\frac{\pi h}{a_0}\right)} \right) \right] \quad h > 0, \tag{9}$$

where γ is the variogram, h the distance between the two corresponding positions, C_0 the nugget effect and C the sill value. It can be seen that a variogram model can consist of multiple components. Often the experimental variogram shows different length scales in different directions, which is called geometric anisotropy. For a linear model, this can be seen as different slopes in different directions, while a global model shows length parameters appearing differently in different directions (Abdlmutalib et al. 2019; Clark 1977b; Li et al. 2018b).

It can be said that the development of the semi-variogram $\gamma(h)$ has a hole effect, when it is not monotonic. Hole-effect models may or may not have sill (Fig. 5).

The three-dimensional space-defined hole-effect model can be given as follows:

$$C(h) = \operatorname{Sin} h/h \quad \text{and} \quad \gamma(h) = 1 - \operatorname{Sin} h/h, \tag{10}$$

where h is expressed in terms of radian. This model has a sill and shows parabolic behaviour at the origin (Fig. 5): $\gamma(h) = h^2/6$, $h \to 0$. The hole-effective model has an amplitude, α, the effect of the hole. If divided by the sill value, the minimum value of the covariance $C(0)$ is $\alpha = |\min C(h)|/C(0)$. The amplitude value for the model given in Eq. 10 is $\alpha = 0.212$ and $r \simeq 4.4934 \simeq 3\pi/2$ The maximum amplitude of an isotropic hole effect is observed in three-dimensional space. If an experimental hole effect has an amplitude greater than 0.212, then the hole effect is either not significant or consists of the fluctuation of the experimental SV, i.e. it is not present in all directions of the three-dimensional space.

If you want to get a strong hole effect, then you just need to use a positive hole-effect definition in one dimension,

$$\gamma(h) = 1 - \cos h. \tag{11}$$

In this case, the relative amplitude α is equal to 1 and superior to 0.212. The cosine model $C(h) = \cos h$ is not positively defined in the three dimension, and so its use should be limited to a specific direction. In the model represented by Eq. 11, the amplitudes of oscillations are periodic without decrease. The periodic components of the changes may appear on experimental SVs as a hole effect. The illustration of two different states of mineralization in an ore body can be given as an example of this explanation (Fig. 6). If this sequence is not isotropic—it is usually anisotropic—then the hole effect is only formed in certain directions, for example, the vertical orientation is the pseudo-periodic sequence of horizontal stratification as seen in Fig. 6.

If Fig. 6a is examined for smaller points, then the vertical SV shows a hole effect with an amplitude greater than 0.217. The apses b_1 and b_2 of the oscillations differ according to
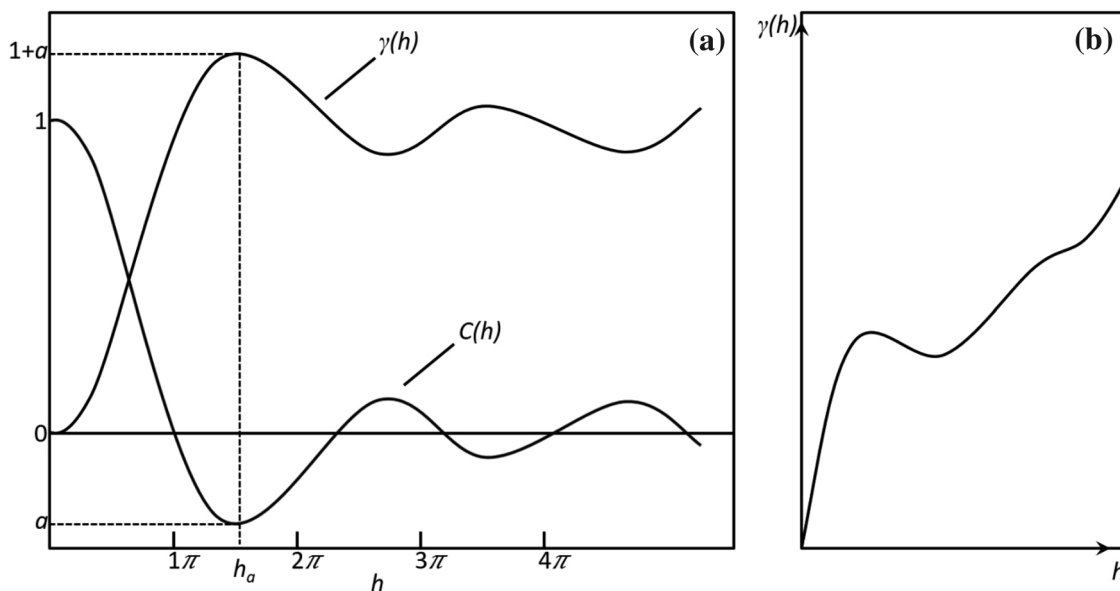

Fig. 5 Hole-effect model, **a** with sill, **b** without sill (modified from (Journel and Huijbregts 1978))
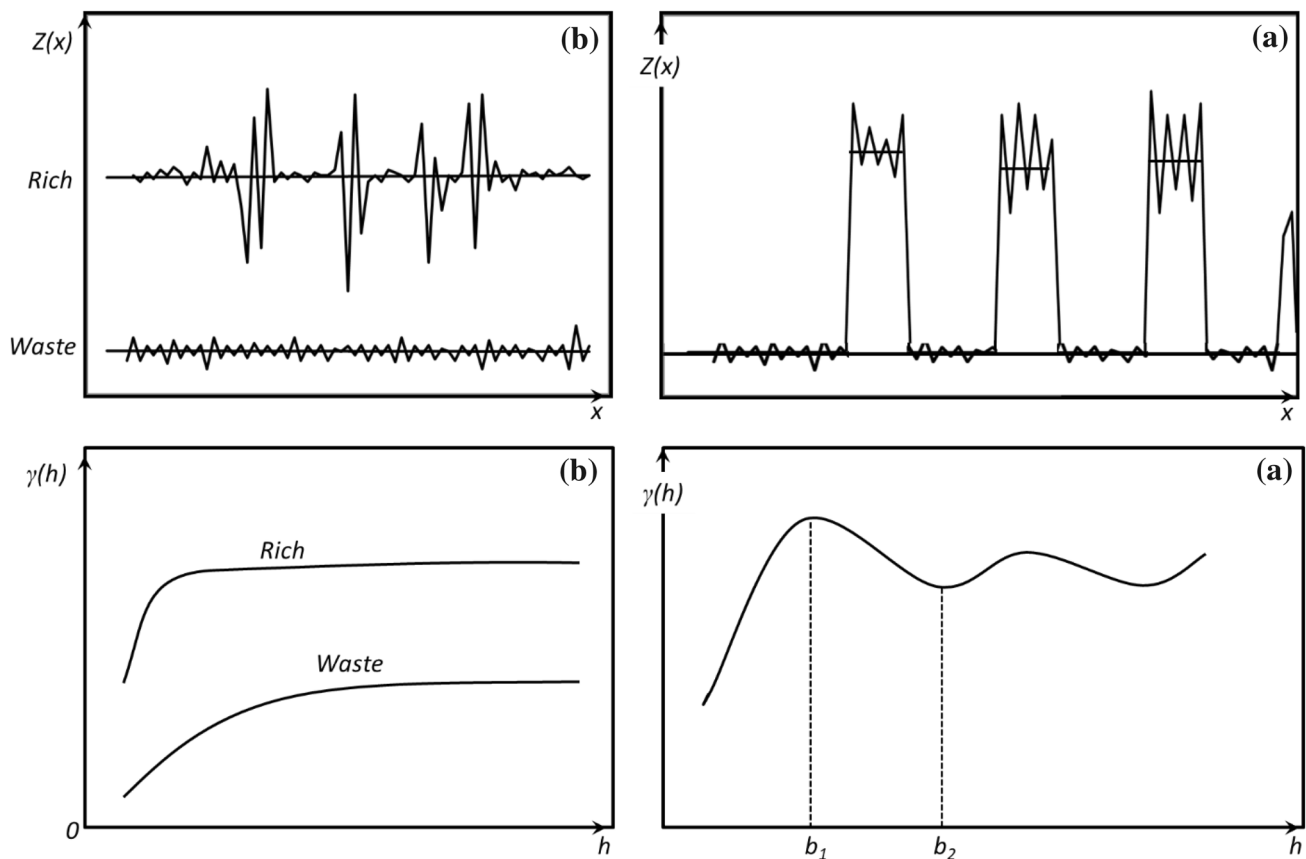
Fig. 6 The drawings are examples of **a** vertical direction and **b** horizontal direction hole (wave) effects (modified from (Journel and Huijbregts 1978))

their settlements in the waste stratum. Finally, the hole effect can also be due to an artificial periodicity of the data (Journel and Huijbregts 1978; Ma and Jones 2001).

Practical difficulties of the semi-variogram

A classical SV is defined as a half-square difference of two measures separated by this distance for any distance h. For a range of distances, a quasi-square difference arises as a theoretical function called an SV, while h varies from zero to the maximum possible distance in the study area. The SV model is an estimate of this theoretical function, which is calculated from the limited number of samples. The SV model can make reliable estimates for small distances when the distribution of sample points within the region is regular. As the distance increases, the number of data pairs decreases for calculation of the SV, which means less reliable estimation at larger distances (Şen 1998b).

The SV assumes that the regional variable is stationary and that the sample locations are distributed regularly. However, in most natural phenomena, the sample locations are scattered irregularly in the region, so that objective

estimation of the SV is not possible. Some distances are closer than others, and accordingly the SV estimates of these points are more reliable than others. Hence, there is great heterogeneous reliability in the SV. As a result, the reliability of the semi-variogram model varies with distance. Such a situation is caused by incompatibilities and experimental fluctuations in the model. To give a consistent pattern to the SV model, different researchers used different personal methods as follows:

1. Some researchers have proposed grouping the data within distance classes of equal length to construct a semi-variogram model. However, the grouping of data pairs in the classes leads to smoothing of the model semi-variogram associated with the basic theoretical SV (Journel and Huijbregts 1978). If the number of distances falls into a certain class, the average of the semi-square differences in this class is taken as the characteristic semi-square difference for the middle point. The effect of outliers is partially reduced, but not fully corrected by the averaging process (Clark 1977a, 1979c; Ma et al. 2001; Şen 1989).

2. To reduce the variability in the semi-variogram, the researchers classified the distances observed among the samples in the variable length classes. This acceptance was also determined by the size of the class, the constant number of pairs of samples falling in each class. The mean value of distance and semi-square differences were used for classification as a representative point of the sample semi-variogram. This method, however, resulted in inconsistency in the sample semi-variogram model for the choice of the number of pairs of m falling into each class. The researchers observed that the data gave a distinguishable shape with $m = 1000$ selection (Şen 1989). The choice of fixed numbers of pairs is individual, and additionally the average processing corrects the variability in the experimental semi-variogram. As a result, the SV cannot provide a correct variable test, because it cannot provide wide frequency changes (Shurtz 1983; Vidal Vázquez et al. 2005). The above methods basically have two general characteristics as the arithmetic average method for the prefixing of the fixed number of pairs or for the difference in class lengths and the distances for the half-squares. In more general cases, the model needs a personal decision; otherwise, it may cause unrepresented SV values. In classical statistics, in the case of only symmetric distribution data, the mean value is best estimated; otherwise, the mean is irrelevant. To overcome these disadvantages, Şen (1989) developed the concept of cumulative semi-variogram (CSV).

Cumulative semi-variogram (CSV)

The CSV technique, which has several advantages over classical methods for determining spatial dependence and regional variability, has been proposed by Şen (1989) as an alternative to Matheron's classical SV technique (Matheron 1963, 1970).

A regional variable represents changes in the space according to the time and location (Delbari and Afrasiab 2014; Liu et al. 2014; Niksarlıoğlu et al. 2015). Temporal and regional developments are controlled by temporal and spatial correlations. If the measurements are made at regular intervals, the whole theory of time series would be sufficient to make the time modelling, simulation and prediction (Karacan 2012; Lü et al. 2012; Tarawneh and Şen 2012; Vázquez et al. 2010b; Zelenika and Malvić 2010). The problem is that measurements in irregular locations are transferred to regular grid points or to any unmeasured point. If the regional dependency structure can be determined effectively, then in any future work, numerical forecasting can be done successfully at any location based on measurement locations. For this purpose, regional covariance and SV functions include field weight functions to account for spatial correlation of the phenomenon under consideration

(Bonnot et al. 2010; De Assis et al. 2010; Mirás-Avalos et al. 2009; Vázquez et al. 2009, 2010a; Yamamoto and Chao 2009). The covariance method requires that the distribution of the regional variable conforms to the Gaussian distribution. The SV model cannot provide a clear model of regional correlation structure. However, the CSV method is used at this point, which does not include these deficiencies (Demir et al. 2009; Nirala 2008; Saghafian and Bondarabadi 2008; Şen 1997; Şen and Şahin 2001; Zas et al. 2007; Zhao et al. 2007).

The CSV model is a graph showing the relation of consecutive half-square difference totals of the order of increasing values of the distances from all possible positions of sampling positions in a region. In short, the CSV is the consecutive sum of the SV values, which provides a non-decreasing distribution diagram. Thus, a non-decreasing CSV function gives several important clues about the behaviour of the regional variable. This process is especially useful when the sampling points are well distributed within the study area. The CSV has all the advantages of the classical SV. All of the models created in the SV can be easily generated with the CSV, which is considered the best tool for defining theoretical models for space diversity. The standardization of the CSV provides an essential condition for defining regional stationary (probabilistic) models (Al-Khashman and Tarawneh 2007; Leptoukh et al. 2007; Meddaugh 2006; Olea 2007; Öztopal 2006; Pardo-Igúzquiza and Dowd 2004; Şahin and Şen 2004; Şen and Şahin 2001; Vidal Vázquez et al. 2007).

The cumulative semi-variogram, which provides a measure of regional connectivity through two closer locations, takes smaller values at these locations where the regional event is more linked. CSV is obtained by applying the following steps:

1. The distance d_{ij} ($i \neq j = 1, 2, …, m$) between each possible pair of scattered measurement positions is calculated. For example, if the number of sample locations is n, then $m = (n − 1)/2$ there is distance value.

2. For each d_{ij} distance, the relevant quadratic differences of the regional variable data, D_{ij}, are computed. For example, if the local variable d_i has values Z_i and Z_j at two different positions within the distance j, then the half-frame difference, $D_{ij} = \frac{1}{2}\left(Z_i - Z_j\right)^2$, happens. Starting sequentially from the smallest distance, the consecutive sum of the squared differences is taken to the greatest distance. This method will provide a non-decreasing function.

3. The distance values are plotted against the CSV values, where the result is similar to the following CSV function (Şen and Şahin 2001). The combined presentation of the semi-variogram and the semi-variogram is shown in Fig. 7.
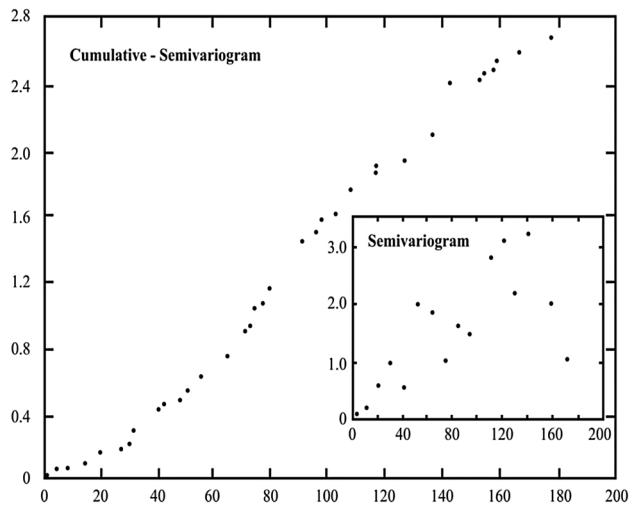
Fig. 7 Representation semi-variogram and cumulative semi-variogram (Şen 1989)

As can be seen from the graph, the SV does not provide clear information about the behaviour of the regional variable, but provides clear information from the CSV graph. In any embodiment, the CSV has the following characteristics:

1. CSV is a non-decreasing function. However, the local flat parts in the graph refer to the dependence of the regional variability at certain distances. That is, the same value can be observed in two positions with h spacing.
2. The slope of the theoretical CSV at any distance indicates the dependence between the pairs of regional variables at the separated distances. During this distance change, the existence of local dependency can be understood by an example CSV function.
3. The CSV model expresses small dependencies between pairs of data that cannot be determined by the classical SV due to the average.
4. The CSV model has objective basis, because it does not require a distinction between distance classes (Şen 1989). The CSV function estimates the value of the regional variable at a location using the standard weight function. Later based on the CSV, Şen (1998b) developed the point cumulative semi-variogram (PCSV) technique to measure the point properties of the diversity in any region.

Point cumulative semi-variogram (PCSV)

The PCSV method, which is developed to quantify the regional changes and is derived from the CSV, is used to search for distributions of the variables around the stationary station (Külahcı 2016b; Niksarlıoğlu et al. 2015;

Tarawneh 2015). In other words, the PCSV refers to the local effect of all other locations within the study area on a particular location. Thus, the number of PCSV values equals the number of stations. Hence, comparison of locations with each other is possible and related regulations provide useful information on the heterogeneity of the variable (Delbari and Afrasiab 2014; Külahcı et al. 2008; Lü et al. 2012; Şen 1989, 1998b; Tarawneh and Şen 2012; Vázquez et al. 2009, 2010a; Yamamoto and Chao 2009). The acceptance of the SV proposed by Matheron (1963) is based on stationarity and equilibrium. In the absence of stability, the relation between random scattered points cannot be examined with an SV approach. The PCSV, proposed by Şen (1998b), explains the relation between the point and field according to the absence of stability and the random distribution of points (Saghafian and Bondarabadi 2008; Şen 1989).

Structural variability in any event within a domain can best be measured by comparing the relative change between the two positions. For example, if the local variables Z_i and Z_{i+d} have measured values separated by distance d, then the relative variability can simply be written as $(Z_i - Z_{i+d})$. To measure the degree of regional variability, the variance and correlation technique cannot express accurately regional dependence due to unusual distribution functions or irregularity of sample locations, although it is frequently used in the literature. All techniques such as classical variogram and autocorrelation require equally spaced data values. However, in practical studies, positions are frequently located irregularly. The CSV method overcomes all these disadvantages, but provides an overview of what happens. It does not refer to the effects of a particular location. The PCSV method, therefore, takes into account the effects of a certain positional circumstance from its predecessor (Külahcı and Şen 2009b; Öztopal 2006).

The PCSV can be defined as the sum of the half of the difference squared line from small to large in the distance. It is applied to air pollution data by Şen (1998a), and to wind speed and energy by Şen and Şahin (1998). If the PCSV value in the kth station is denoted by V_k, the mathematical expression is given by the following expression:

$$V_k = \frac{1}{2} \sum_{i=1}^{n-1} (Z_k - Z_i). \tag{12}$$

Here, the radius of influence Z_k denotes the value of the regional variable at the requested (pivot) station and Z_i ($i = 1, 2 ..., n, i \neq k$) at the other stations, where the total number of stations is n. The PCSV graph shows the variation of calculated V_k values against distance. To obtain the PCSV graph, the following operations must be performed:

1. The distances between the selected station k and the other stations ($i = 1, 2, \ldots, n; \; i \neq k$) are calculated. If there are n positions, $n - 1$ is the difference in distance.
2. For each pair, there are half-square differences between the data values. In this way, each distance will have its own half-square values $(Z_k - Z_i)/2$, where Z_k and Z_i are the values of the regional variable in the corresponding region and i, respectively.
3. The distances are sorted from small to large and the sum of consecutive half-square differences are calculated against the distance. This method gives a non-decreasing function of the PCSV example at the location. The mathematical expression is given as

$$\gamma(d_i) = \frac{1}{2} \sum_{i=1}^{n-1} (Z_k - Z_i)^2. \tag{13}$$

4. For the given PCSV, the previous steps are applied taking into account the different relevant areas.
5. By placing the computed $\gamma(d_i)$ values vertically and the distances corresponding to them at the horizontal axes, a PCSV scattering diagram is obtained.
6. As a result of fitting the least squares method of a curve to this scatter diagram, the theoretical PCSV model is obtained, that is, the function of changing the regional variable by distance.

With the help of this technique, it is possible to estimate various properties such as radius of influence, homogeneity, independence and correlation. The main features of the PCSV graph defined by Eq. 12 are:

1. The PCSV is an increasing function of distance.
2. The scatter diagram between the PCSV and the distance gives an idea about the dependence between these two stations from the slope between the two points. If the slope is zero, there is full dependency between the two stations, i.e. the correlation coefficient is 1. The dependence will decrease as the slope increases.
3. Small scattering of the points on the PCSV graph indicates that the examined variable shows a homogeneous structure around the station.
4. The PCSV graph gives the "radius of influence" of the distance station at which the change starts to stabilize with the derivation help of the best curve to be fitted to the scatter diagram.

Using the activity values measured in each station where the sediment and water samples were taken, the PCSV values were obtained on a special position, expressing the regional effect of all other locations within the study area (Şen 1989). Then, using the PCSV–distance data, graphics were obtained which gave information about the regional behaviour of the variable. These charts were fit with the curves with Matlab computer program. Fitted curves were evaluated in terms of sill, nugget and impact radius, which are the basic parameters of the semivariogram models. As a result of these evaluations, it was decided that the regional behaviour of each station was suitable for each station based on the similarities between the obtained curves and the variogram models.

Research area

Uluova is a tectonic-based depression plaster situated in the Southeast Taurus Fold System at the Upper Euphrates Division of the Eastern Anatolia Region. The main geomorphological units in the study area are mountainous areas, low and high platelets, plains, pond cones and fans, skirt plains, valleys, stream shapes and straits. The Uluova region is bounded by Hasret Mountain from the north and the Asker Mountain from the north-east. The height of Hasret Mountain reaches 1621 m in the west and drops to 1200 m in the east near the Murat Bosphorus. Uluova is surrounded by Kuşakcı (1908 m), Çelemlik (1647 m) and Mastar (2171 m) mountains extending from the south in a row from the west to the east. Because of the low permeability, weak vegetation and slope over the southern slopes of Harput Plateau and Hasret Dağ, northern slopes of Kuşakçı, Çelemlik and Mastar Mountains overlooking Uluova, the rivers in these areas are short in length and have high bifurcation rates. Due to the irregular but frequent rainfall occurrences, the amount of water passing to the surface stream is high, so the rivers carry plenty of material. They accumulate the material they carry at the edge of the plain base, depending on the increase in permeability and the slope failure. These sink areas are the water reservoir. The Uluova region is about 35 km long and 10–12 km wide with a surface area of 360–370 km². A large part of this area is covered by the Keban Dam Lake with an area of about 250 km². The altitude of the reservoir varies between 845 and 1000 m (Şengün 2008).

The sediment samples used in the application part of this study are taken from 19 different stations in the lake sediment. The 19 sampling stations are shown in Fig. 8. Water samples are taken from 14 different stations from the lake surface. Distribution of the stations to the lake surface is shown in Fig. 9.

Results and discussion

As a result of the analysis of sediment samples, the ^{40}K activity concentration is seen as 0.004 Bq/g on average. The values of the sediment sample stations are shown in Table 4. The highest ^{40}K activity concentration is at station 11 with
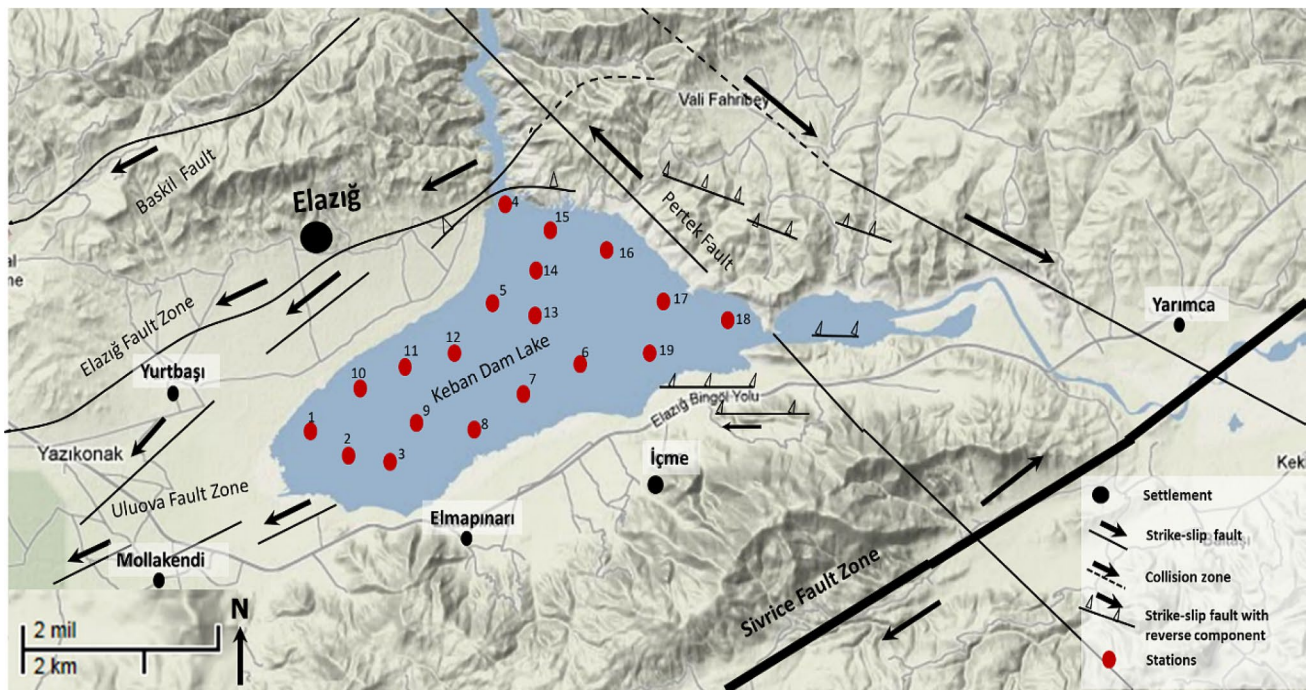
Fig. 8 Distribution at lake surface of the 19 stations where soil samples are taken
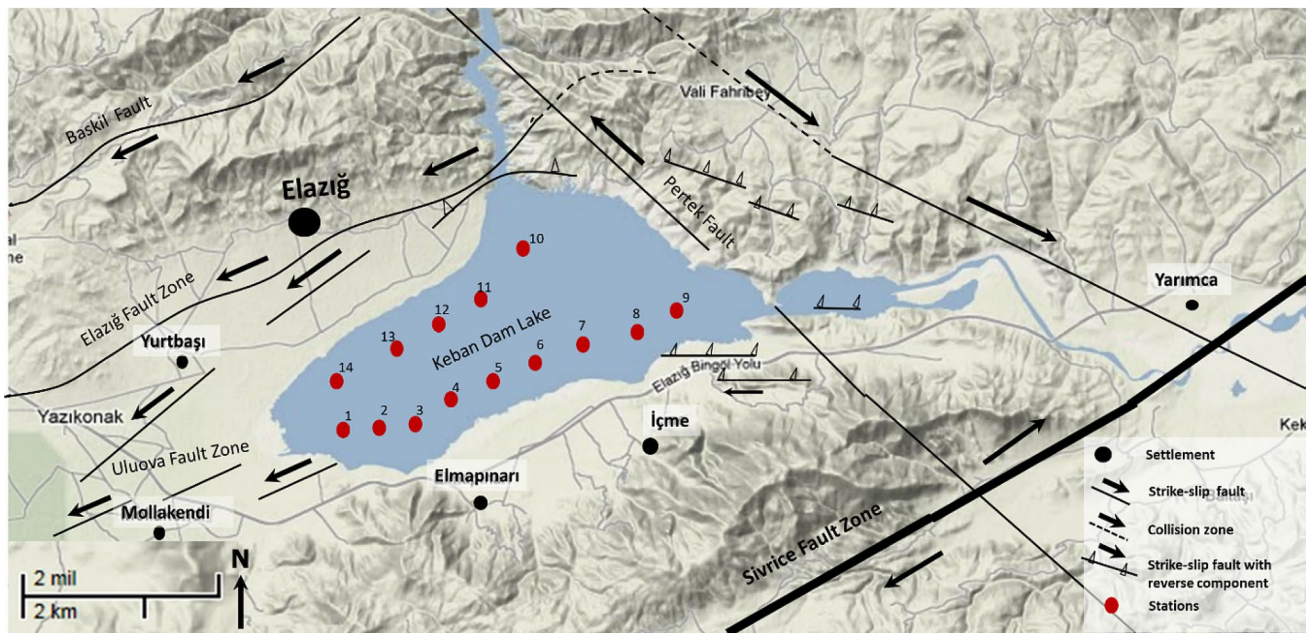

Fig. 9 Distribution at lake surface of the 14 stations where water samples were taken

0.011 Bq/g and the lowest activity concentration is at station 1 at 0.0001 Bq/g. The ^{40}K lake sediment distribution and the location of the stations are clearly visible in Fig. 10. ^{40}K is present in intense amounts in the southwest part of the dam. In the south-western part of the settlement, the use of

potassium fertilizer in agriculture may have resulted in an increase of ^{40}K. In the northern and eastern parts of the dam, there is a low amount of ^{40}K.

The PCSV–distance graphs of ^{40}K values are modelled as in Fig. 15 and the results are given in Table 2. The 3rd

Fig. 10 Iso-radioactivity map of K-40 soil samples
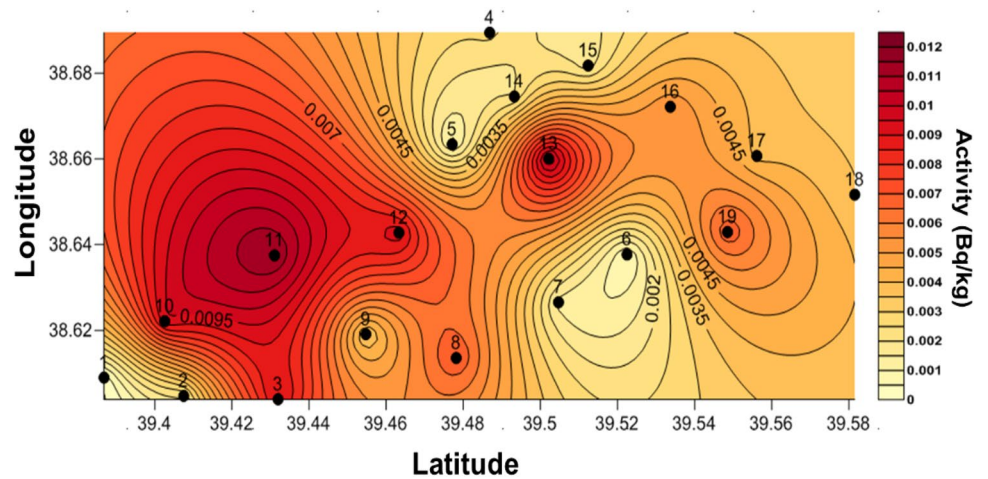
and 5th station model is of type *C*; 9th, 11th, 12th and 14th station model is of *E*; 17th and 18th stations model is of *F*; 4th, 6th, 7th and 16th station correspond to model *H*; stations 8th, 15th, and 19th to model *I*; and finally stations 13rd and 10th correspond to models *B* and *G*, respectively. The PCSV–distance charts for these stations are shown in Figs. 1–19 in Appendix 1 in ESM. Model *E*, representing four stations (9th, 11th, 12th and 14th), has a nugget value on the *y-axis* with an asymptotic sill value. The fact that the graphics have a nugget value means that there is a high ^{40}K activity concentration at the point at station locations. The relationship of these matching stations to other stations is very high. The asymptotic sill value means that the ^{40}K activity concentration decreases as you move away from the station and approaches zero at very large distances.

Model *E* has a radius of influence that ranges from 10 to 18 km. The radius of influence equals the distance at which the variable is known effectively. Model *E* indicates that the variable has a weak change at short and long distances and strong at medium distances. Model *H* represents stations 4th, 6th, 7th and 16th, by a linear model that intersects the

x-axis without a sill value. The fact that this model does not have a sill value means that the variance is homogeneously distributed around the stations matching this model, and this means further that the distribution is uniform. The *I* model represents three stations (8th, 15th, 19th), again by a linear model with a nugget value on the *y-axis* contrary to the *H* model. The presence of nugget value on the *y-axis* means that the ^{40}K activity concentration may be higher around the model-matching stations.

The values of ^{40}K activity concentration of water samples are shown in Table 3. According to this table, the ^{40}K activity concentration average is 6.68 Bq/l. Station 1 has the highest activity concentration at 12.44 Bq/l and station 2 has the lowest value at 1.93 Bq/l. The distribution of ^{40}K to the lake surface is shown in Fig. 11, where the northern section of the lake and the south section are more abundant than the other sections of the lake, in terms of ^{40}K activity concentration. A lower ^{40}K activity concentration is seen in the middle sections.

PCSV–distance plots of values of ^{40}K are shown in Figs. 20–33 in Appendix-1 in ESM. These graphs are

Table 2 Grouping of stations into appropriate models

Radioisotope					
Model	^{40}K sediment	^{40}K water	^{232}Th sediment	^{232}Th water	^{238}U sediment	^{238}U water
A	1, 2	13	19	2, 4, 12		12, 13, 14
B	13	1, 2, 3, 5, 12	6, 11, 12	1, 3, 5, 11	5, 6, 13, 15, 17, 18, 19	2
C	3, 5	8	–	–	–	6, 8
D		11		–	8, 9	
E	9, 11, 12, 14	4, 6, 10	5–10, 13, 14, 17, 18	6, 7, 8	7, 11, 12	1, 3, 4, 5, 7, 11
F	17, 18	–	–	–	–	10
G	10	7, 9,	1, 3, 4	–	1, 2, 3, 10	9
H	4, 6, 7, 16	–	2	10	4, 14	–
I	8, 15, 19	–	15	9	–	–
J	–	14	16	13, 14	16	–

grouped based on the models in Fig. 12. According to this, 1st, 2nd, 3rd, 5th and 12th stations are assigned to model *B*; 4th, 6th, and 10th stations to model *E*; 7th and 9th stations to model *G*; 13th, 8th, 11th, and 14th stations to *A*, *C*, *D*, and *J* models. Model *B* representing five stations (1st, 2nd,

3rd, 5th, and 12th) cuts the distance axis and reaches sill value at long distances. In addition, model *B* has a radius of effect ranging from 8 to 12 km. The intersection of the model's distance axis means that the ⁴⁰K activity concentration at these distances is low and has not changed. Having

Table 3 Radioactivity levels of water samples

Station no.	Latitude	Longitude	Sample volume (L)	^{238}U (Bq/L)	^{232}Th (Bq/L)	^{40}K (Bq/L)
1	38,6049	39,4087	0.1	32.376	9.398	12.442
2	38,6049	39,4307	0.1	2.611	4.003	1.934
3	38,6097	39,4476	0.1	21.410	13.923	4.456
4	38,6117	39,4687	0.1	11.488	4.351	5.717
5	38,6255	39,4755	0.1	8.877	5.3951	8.407
6	38,6233	39,4997	0.1	3.133	2.088	6.726
7	38,6346	39,5195	0.1	2.089	1.914	6.389
8	38,6362	39,5437	0.1	17.233	4.873	7.987
9	38,6447	39,5691	0.1	8.877	8.528	4.876
10	38,6723	39,4851	0.1	10.444	7.657	10.425
11	38,6511	39,4490	0.1	6.789	5.743	3.951
12	38,6388	39,4255	0.1	21.410	9.572	4.12
13	38,6277	39,4071	0.1	13.577	1.740	6.894
14	38,6152	39,3857	0.1	10.444	2.262	9.248
Average				12.19	5.81	6.680

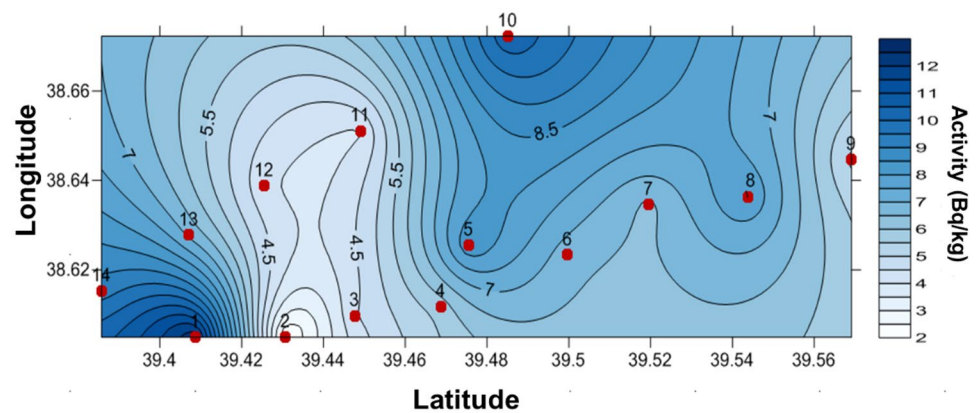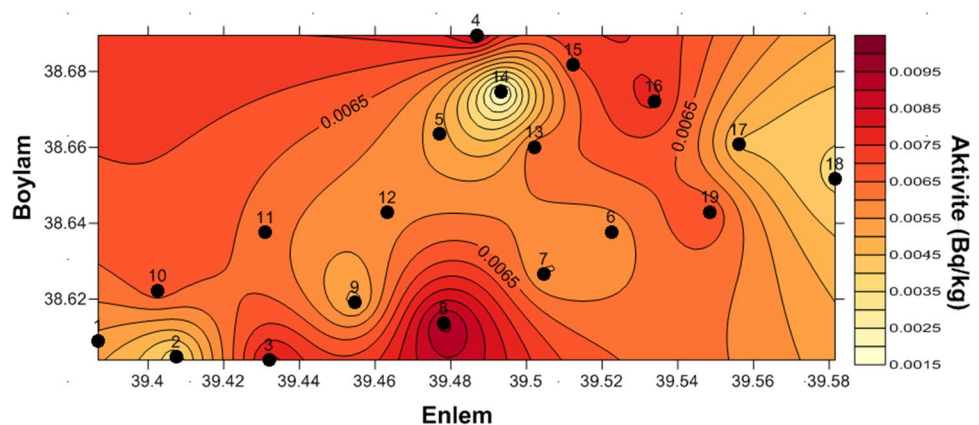**Fig. 11** Iso-radioactivity map of K-40 water samples

Fig. 12 Iso-radioactivity map of Th-232 soil samples

a radius of influence between 8 and 12 km indicates that these stations are affected by other stations. Long distance sill means that the ^{40}K activity concentration shows a weak change over long distances. Model E, which represents three stations (4th, 6th, and 10th), has a nugget value on the PCSV axis and has a sill value. This model is in the form of a Gaussian curved line with increases between 5 and 10 km, and 0 and 5 km showing stagnation afterwards. Nugget value means that the variable may be influenced by the geological structure of the lake. The sill showing the peak value of model E determines the radius of influence of the variable and the radius of effect is around 10 km.

The ^{232}Th activity concentration values of samples taken from 19 different stations from the bottom sediment of the lake are shown in Table 4, where the average of ^{232}Th stations is 0.005 Bq/g. Station 8 has the highest ^{232}Th activity concentration with the lowest at the 14th station. The distribution of stations and ^{232}Th is shown in Fig. 12, where the northern and southern parts of the lake have a higher ^{232}Th activity concentration than the middle parts. The materials transported from mountainous areas around the lake may have caused an increase of ^{232}Th in these areas. For this reason, it can be shown that the mountainous areas around the study area are volcanic (Külahcı 2005).

The PCSV–distance graphs obtained from the values of ^{232}Th and the distances between stations are shown in Figs. 1–19 in Appendix-2 in ESM, where these graphs are grouped according to the models shown in Fig. 15.

According to this, the 5th, 7–10th, 13th, 14th, 17th, and 18th stations accord with the model E; 6th, 11th, and 12th stations correspond to model B; 1st, 3rd and 4th stations to model G; stations 19th, 2nd, 15th and 16th correspond to model A, H, I, and J, respectively. The model E, which represents a large part of the stations (total 9 stations), resembles a Gaussian curve. However, model E has nugget value plus sill value. These stations have a radius of influence of 9–14 km, which means that the activity concentration of ^{232}Th lost its influence after 14th km. Model E has a nugget effect on the *PCSV axis*. The nugget value of model E means that there is a lot of transport in the locations where these location patterns have influencing. Model G, which represents three stations, does not have a sill value with nugget value. Model G shows an exponential increase. This means that stations that conform to model G are increasingly influenced by their surroundings. The ^{232}Th densities of these stations also mean that they affect the ^{232}Th densities of other stations as well. Model B with three stations intersects the distance axis and has an asymptotic sill value. This is a feature that distinguishes model B from other models. This means that there is a weak interaction between stations and a strong interaction afterwards until the distance of the curve is shorter than the distance.

The ^{232}Th values at 14 different sample stations at the lake surface are shown in Table 3. Measurements and calculations show that the station has the highest ^{232}Th in surface water samples at the 3rd station with 13.92 Bq/l.

Table 4 Radioactivity levels of sediment samples

Station no	Longitude	Latitude	EPW (g)	FPW (g)	^{238}U (Bq/g)	^{232}Th (Bq/g)	^{40}K (Bq/g)
1	39,3868	38,6090	1.3420	1.4043	0.01145	0.00534	0.00012
2	39,4075	38,6047	1.2512	1.4217	0.00289	0.00360	0.00205
3	39,4320	38,6039	1.3703	1.5377	0.00727	0.00824	0.00916
4	39,4869	38,6895	1.3466	1.4047	0.02011	0.00882	0.00268
5	39,4771	38,6634	13655	1.4813	0.01128	0.00522	0.00080
6	39,5225	38,6377	1.1843	1.3953	0.00917	0.00569	0.00042
7	39,5047	38,6266	1.2404	1.3947	0.00670	0.00545	0.00133
8	39,4782	38,6136	1.3264	1.4917	0.01123	0.00975	0.00709
9	39,4547	38,6191	1.2944	1.3973	0.01045	0.00476	0.00334
10	39,4026	38,6221	1.1700	1.3160	0.01299	0.00685	0.00944
11	39,4311	38,6375	1.1445	1.3253	0.01443	0.00627	0.01159
12	39,4633	38,6428	1.2621	1.3443	0.01583	0.00580	0.00934
13	39,5022	38,6600	1.3374	1.4523	0.00290	0.00638	0.01061
14	39,4933	38,6746	1.3739	1.4823	0.01763	0.00151	0.00199
15	39,5124	38,6818	1.3836	1.4200	0.03101	0.00696	0.00172
16	39,5337	38,6722	1.3855	1.5013	0.00776	0.00766	0.00544
17	39,5561	38,6607	1.2771	1.4393	0.01059	0.00441	0.00384
18	39,5816	38,6516	1.3593	1.4903	0.01220	0.00383	0.00355
19	39,5485	38,6429	1.3499	1.4720	0.00462	0.00696	0.00699
Average					0.011	0.005	0.004

EPW empty planchette weight, *FPW* full planchette weight

The 13th station has the lowest ^{232}Th activity concentration at 1.74 Bq/l. The average of ^{232}Th for the 14th station is 5.81 Bq/l. ^{232}Th densities of the 5th and 11th stations have average values. The stations where the surface waters are taken and the map of the ^{232}Th activity concentration are clearly shown in Fig. 13. According to this, the south-west part of the lake is richer in terms of ^{232}Th activity concentration than the other parts. Usually, the central part of the lake has a lower ^{232}Th activity concentration. There may be accumulation in the coastal areas due to the effects of the waves that flow in the openings of the lake and it has high mobility. In addition, the lower activity concentration of ^{232}Th in the north suggests that the ^{232}Th may have drifted southward due to the flow of the river forming the lake.

The graphs plotted against the ^{232}Th concentrations of water samples and the distances of the stations to each other are grouped based on the models in Fig. 15. According to this grouping, the 1st, 3rd, 5th and 11th stations accord with model *B*; 2nd, 4th and 12th stations with model *A*; 6th, 7th and 8th stations with model *E*; 13th and 14th stations with model *J*; 10th and 9th stations conform to *H* and *I*, respectively. PCSV–distance graphs of these stations are shown in Figs. 20–33 in Appendix 2 in ESM. Model *B*, representing four stations (1st, 3rd, 5th and 11th), has a nugget value on the *x*-axis and contains an asymptotic sill value. According to model *B*, the stations have a radius of effect between 7 and 11 km. The radius of the influence is equal to the radius of the field, where the variable is active. Accordingly, the intensity of ^{232}Th has a strong influence at distances less than 7–11 km from stations that match model *B*. After this distance, the effect diminishes and approaches zero. The asymptotic sill value is also a proof that this influence will not be zero, but it will come very close to zero. The model *A*, with three stations of compatibility, has a nugget value on the *PCSV axis* and has an asymptotic sill value. In addition, the model has a radius of influence of 9–12 km. Unlike model *A*, model *B* has a nugget value, which indicates that the variable is under the control of some geological events

at that point. Model *E*, another model representing three stations (6, 7, and 8), resembles a Gaussian curve and has a nugget effect on the PCSV axis and additionally a sill value. Model *E* has a radius of effect of 8–14 km. This gives us information about ^{232}Th's range of water transport.

The ^{238}U of sediment samples has an average activity concentration of 0.011 Bq/g. According to the values given in Table 4, the station with the highest activity concentration of ^{238}U among the received samples is the 15th station, while the station with the lowest value is the 2nd station. The distribution of the stations in the lake and the ^{238}U concentration of the lake are shown in Fig. 14. In the northern part of the lake, the high ^{238}U activity concentration attracts attention. This part of the lake could have reached a high ^{238}U activity concentration with the alluvium carried by the Euphrates River forming the dam. However, the ^{238}U activity concentration at the northern part stations of the lake is about 30–50% higher than the ^{238}U activity concentration of the southern part.

The PCSV–distance graphs obtained from ^{238}U values of sediment samples are divided according to the models shown in Fig. 15 and Table 2. Considering the grouping, the 1st, 2nd, 3rd and 10th stations are assigned to model *G*; 5th, 6th, 13th, 15th, 17th, 18th and 19th stations to model *B*; 8th and 9th stations to model *D*; 7th, 11th and 12th stations to model *E*; 4th and 14th stations to model *H*; and finally the 16th station to model *J*. The PCSV–distance graphs of the stations are shown in Figs. 1–19 in Appendix-3. Model *B*, representing a large portion of the stations, has a nugget effect on the distance axis and an asymptotic sill value. This indicates that the variant is homogeneously distributed to a certain distance and then this homogenization is lost. The model *B* also has a radius of influence of 8–10 km. The radius of influence corresponds to the distance at which homogeneity disappeared. The model *G*, which represents 1st, 2nd, 3rd and 10th stations, has a nugget. Model *G* shows an exponential increase. This increase indicates that the 238U activity concentration increases as the stations go

Fig. 13 Iso-radioactivity map of Th-232 water samples
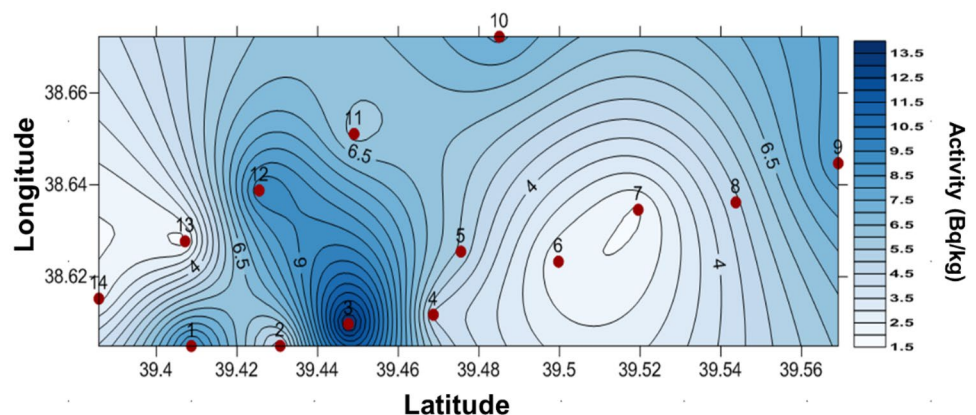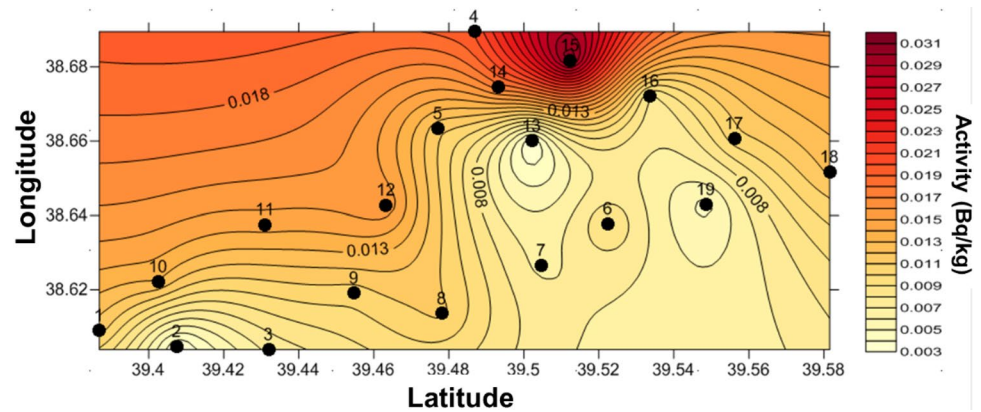
Fig. 14 Iso-radioactivity map of U-238 soil samples

outward. The nugget effect also shows the regional dependence of the distribution and concentration values of 238U.

The ^{238}U activity concentration of water samples taken from the lake surface is 12.19 Bq/l. The activity values of the stations, where water samples were taken, are shown in Table 3. According to the values given in this table, the highest ^{238}U activity concentration is seen in the first station. The seventh station has the lowest ^{238}U activity concentration. Considering the distribution of ^{238}U, it is seen that the stations near settlements have higher values than other places, which is evident in Fig. 16. The fact that stations close to the settlements have a high value of ^{238}U may be due to the large amount of water carried to the lake surface. Moreover, the fact that this region has a plain structure can be used to facilitate the transport of rainwater, so that the ^{238}U transported by the waters may have accumulated in this region.

The PCSV–distance graphs of the ^{238}U water samples are shown in Figs. 20–33 in Appendix-3 in ESM. Stations that match model E have a radius of influence of 6–12 km, where there is also a small nugget effect at these stations, but the variogram value seems to have sill value. The projection of the point reaching the sill value to the axis of distance corresponds to the radius of influence. This shows that the ^{238}U is lower than the range in the wider range of the earth. The nugget effect of the model E shows that the ^{238}U is under an influence around these model-compliant stations. Model A has a lower radius of effect than model E. However, model A has a nugget effect similar to model E. Model C, which represents two stations, has a nugget effect on the PCSV axis. However, in C model, sill or radius of influence is not observed. Model C is proof that ^{238}U has a steady distribution around these model-matching stations.

The values of ^{238}U, ^{232}Th and ^{40}K activity of sediment samples taken from Keban Dam Lake are shown in Table 4, according to which ^{238}U activity has average 0.011 Bq/g.

The relative error in measurements and calculations is in the range of 5–15%. ^{232}Th and ^{40}K activities are determined to be 0.005 Bq/g and 0.004 Bq/g on average, respectively. The ^{238}U activity is approximately 100% greater than the ^{232}Th and ^{40}K activity. The greater activity concentration of uranium is due to the greater part of the natural radioactivity.

The amount of absorbed sediment sample is 12.7 nSv, whereas the world average dose of absorbed dose is 70 μSv, which means that the amount of water absorbed by the waters of lake is below the world average.

The ^{238}U, ^{232}Th and ^{40}K activity values of the water samples taken during the spring period are shown in Table 3, where ^{238}U activity is 12.19 Bq/l on average, ^{232}Th activity is on average 5.81 Bq/l and ^{40}K activity is 6.68 Bq/l. The relative error in the measurements and calculations is in the range of 5–15%. The activity concentration of uranium is high in the water as well as in the sediment. In contrast, the ^{40}K activity concentration is greater than the ^{232}Th activity concentration, which indicates that ^{232}Th is carried in water better than ^{40}K. The amount of absorbed sediment value is below 8×10^{-3} μSv.

The activity values of the samples taken from the sediment are lower than the activity values of the samples taken from the water. During the winter period, the rains coming from the lake are full of material and rain water. For this reason, an increase in the total radionuclide concentration in the spring period is generally expected. In some previous studies, ^{238}U of rock samples was found to have an average of 200 Bq/kg, a ^{232}Th activity of 20 Bq/kg and a ^{40}K activity of 300 Bq/kg (Alatise et al. 2008; Degerlier et al. 2008; Oyedele et al. 2010). This indicates that there is more natural activity in the rock samples than normal. Geographical rocks formations are crumbling to the ground over time. The rock particles that are mixed into the earth are distributed to the
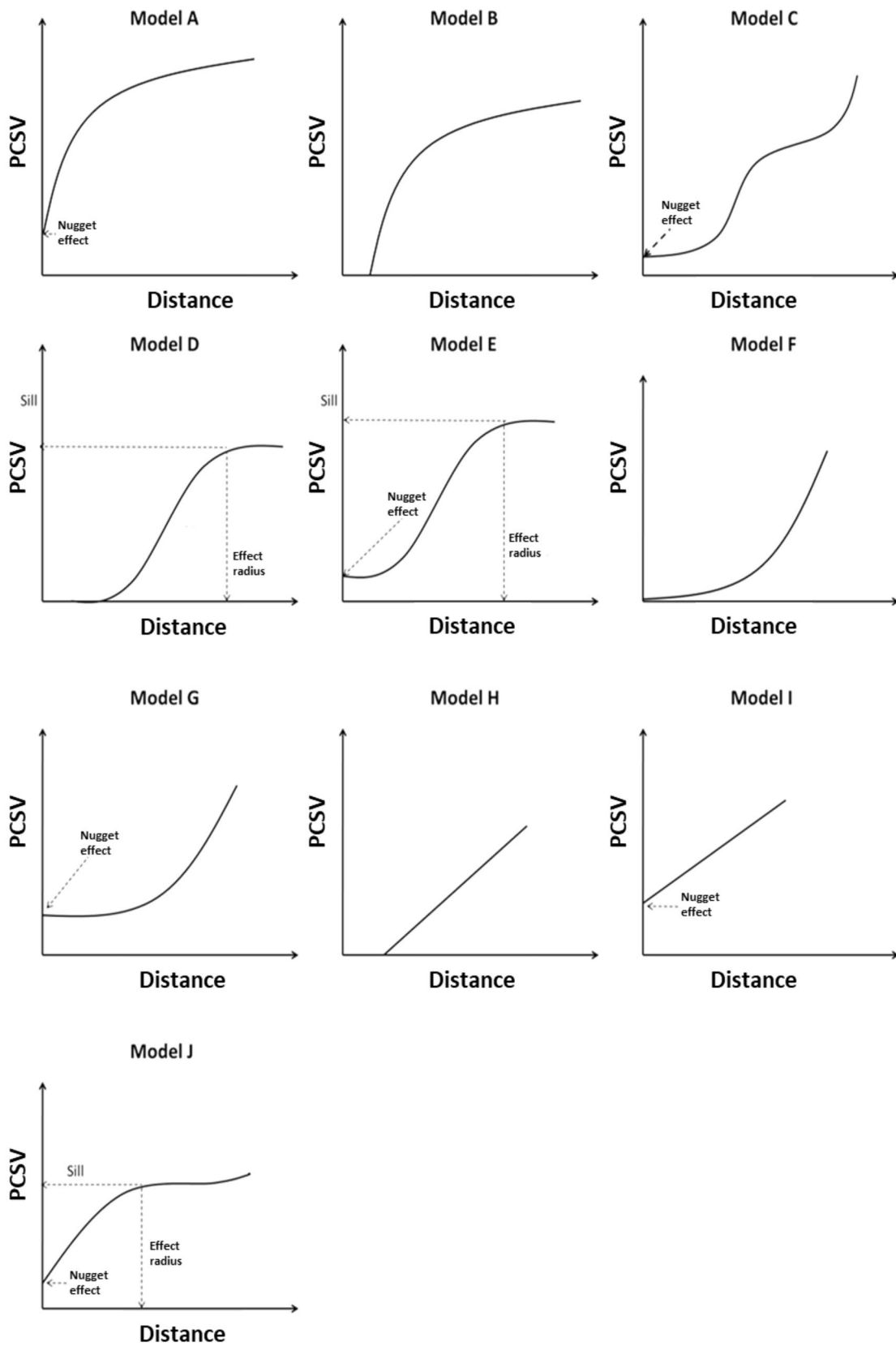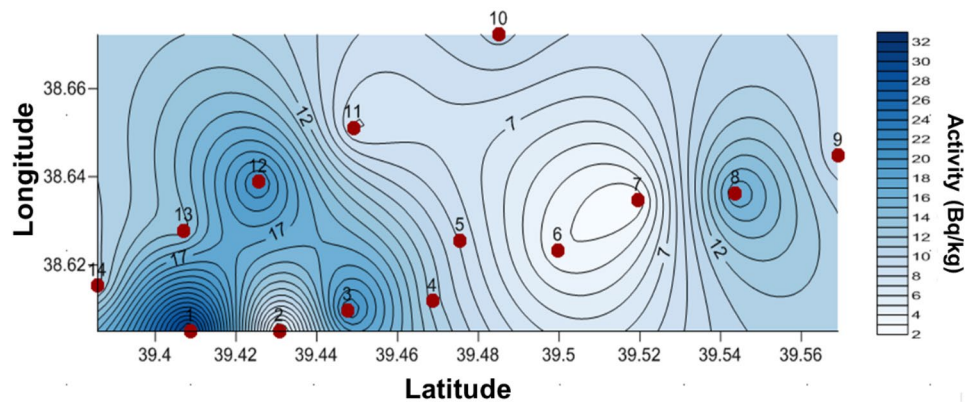
Fig. 15 Point cumulative semi-variogram models proposed in this study

Fig. 16 Iso-radioactivity map of U-238 water samples

earth by the ground waters. Thus, the natural radioactivity is propagated to the earth.

Conclusions

The transport, range and distribution characteristics of uranium-238, thorium-232 and potassium-40, which are the three most important natural radionuclides in the environment, are determined by taking into account the progress of the SV methodology. It is seen that spatial modelling is very effective in solving the problem process. It has been seen that these radionuclides cannot be determined by classical monitoring procedures in the environmental setting. In terms of the variable analysed, it is necessary to know the contribution of each station to other stations. In this study, the contributions of all stations to each other are also determined using the point cumulative SV (PCSV) method. This determination is important in analysing the research area in a homogeneous manner.

In mathematical models and in particular spatial modelling, the facilitating aspect of geology and geophysical applications require a great deal of manpower and time. From the modelling of yeast cells to the modelling of macroscopic systems, it can easily be used in modelling many systems. This modelling technique, which is still available for further development, even though it has a history of about 250 years, now has a rich variety that is almost a sub-branch in geophysics.

In an aquatic environment such as a lake of ^{40}K, the transport range with bottom sediments is detected at a range of 10–18 km. The transport range of the ^{40}K in water is found to be 8–12 km. All these changes show that the "radius of influence" parameter can serve as a radio tracker. For example, it can be seen from this result that the effectiveness of the bottom runoff of the lake is

33% higher than the surface currents. The transport of ^{232}Th along with the bottom sediments is 9–14 km. This result means that the transport cannot be seen after 14th km and other range values can also be interpreted similarly. The range of ^{232}Th in water is determined between 8 and 12 km. The transport of ^{238}U in the bottom sediments is 8–10 km, while the transport of the surface waters is within 6–12 km. The high variation of the range of the surface waters is influenced by the currents. As a result, it has been seen that the spatial modelling methods can be used effectively for the determination of the natural range of the related radionuclides. With spatial modelling techniques, it is also possible to visually observe the changes in the radionuclide concentrations and the transport characteristics. For example, it was determined that the concentration of ^{238}U was higher in the northern parts of the lake than in the southern parts. As it is known, the soil diversity in the earth and the radionuclides concentrations can show very different results in different latitudes and longitudes. The bottom sediments of the Keban Dam Lake Uluova Region, which is chosen as the application area for this review article, are completely clay. The high retaining properties of the clay structure show that the transport of radionuclides is very difficult for regions with such geomorphological characteristics. The initial radionuclide concentrations formed during geological times are thought to be relatively constant due to the conservation of these clay layers. The decrease in activity with radioactive decay is due to the statistical nature of radioactivity. On the other hand, it prevents the transfer of new radioactive particles to the environment due to the high retention of the clay layers. Radon studies conducted by _ENREF_75in this region show that the layers of clay are almost non-penetrating from the bottom of the lake, as very dense clay layers are found. As can be seen in Fig. 17 , very dense clay layers are a major barrier to gas transport in the lake
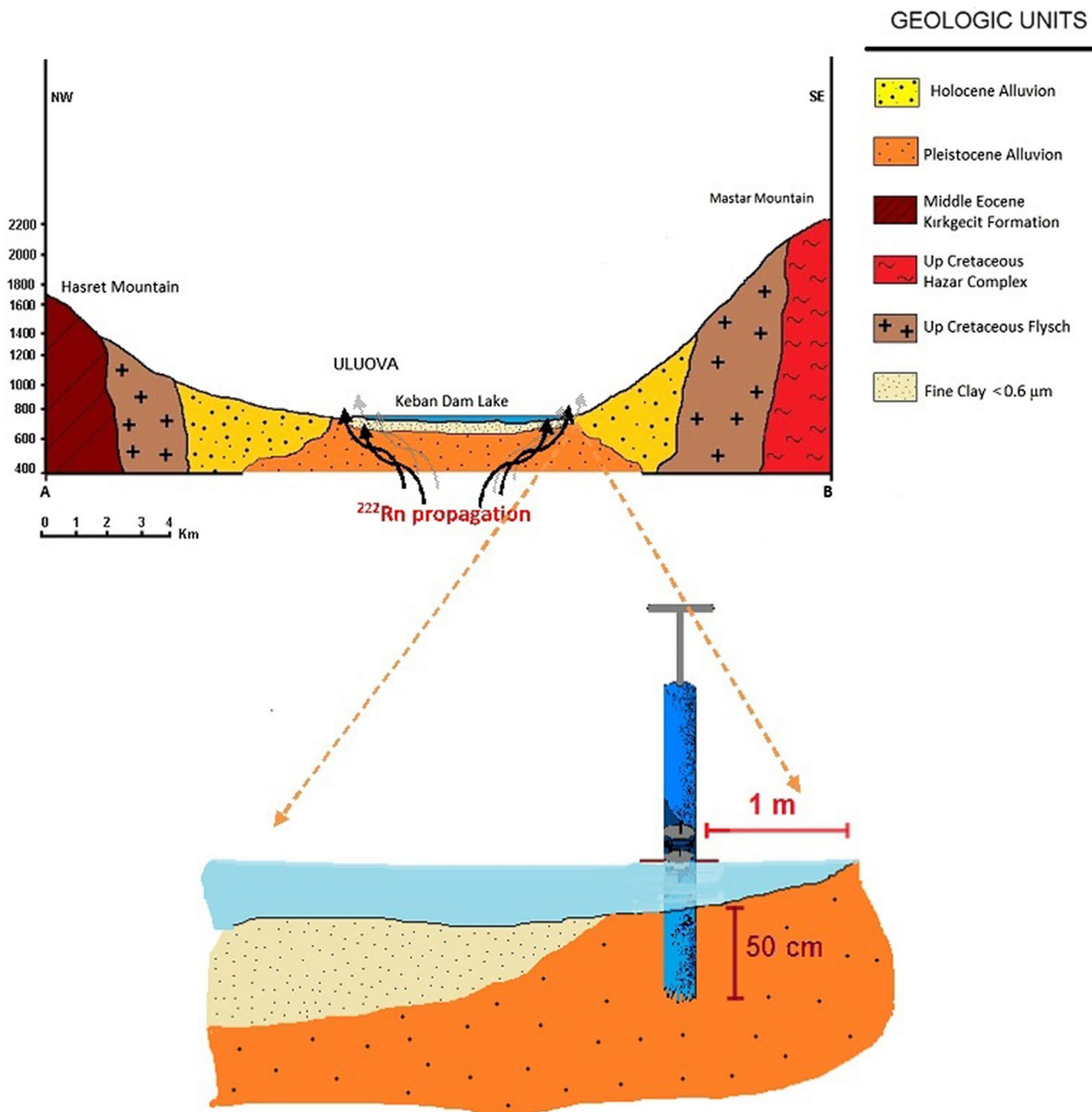
Fig. 17 Geomorphologic units in the study area (Keban Reservoir, Uluova Zone) (modified from Kulahci and Sen (2014) and Şengün (2008)). In the research conducted by Külahcı and Şen (2014), due to the dense clay formation in the region, almost no radon gas leak is observed from the bottom of the lake. For this reason, radon gas sampling is carried out 1 m away from the lake and 50 cm deep

(Kulahci and Sen 2014). At the same time, as mentioned above, the clay layers serve as a trap for horizontal transfers of radionuclides.

References

Abdlmutalib A, Abdullatif O, Abdelkarim A, Yousif I (2019) Factors influencing acoustic properties of carbonate rocks: examples from middle Jurassic Carbonates. Central Saudi Arabia Jafes 150:767–782. https://doi.org/10.1016/J.Jafrearsci.2018.10.005

Adams JA, Osmond JK, Rogers JK (1959) The geochemistry of thorium and uranium. Phys Chem Earth 3:298–348

Alatise O, Babalola I, Olowofela J (2008) Distribution of some natural gamma-emitting radionuclides in the soils of the Coastal Areas Of Nigeria. J Environ Radioact 99:1746–1749

Al-Khashman OA, Tarawneh QY (2007) Spatial prediction model and its application to chemistry of atmospheric precipitation in Jordan. Atmos Res 84:399–409. https://doi.org/10.1016/J.Atmosres.2006.10.002

Antoine M, Javaux M, Bielders C (2009) What indicators can capture runoff-relevant connectivity properties of the micro-topography at the plot scale? Adv Water Resour 32:1297–1310. https://doi.org/10.1016/J.Advwatres.2009.05.006

Arslan H (2017) Determination of temporal and spatial variability of groundwater irrigation quality using geostatistical techniques on the coastal aquifer of Çarşamba Plain, Turkey, from 1990 to 2012. Environ Earth Sci. https://doi.org/10.1007/S12665-016-6375-X

Atwood DA (2013) Radionuclides in the environment. Wiley, New York

Attendorn H-G, Bowen R (2012) Isotopes in the earth sciences. Springer

Banks D, Royset O, Strand T, Skarphagen H (1995) Radioelement (U, Th, Rn) concentrations in norwegian bedrock groundwaters. Environ Geol 25:165–180. https://doi.org/10.1007/Bf00768546

Batuk ON, Szabo DV, Denecke MA, Vitova T, Kalmykov SN (2013) Synthesis and characterization of thorium, uranium and cerium oxide nanoparticles. Radiochim Acta 101:233–239. https://doi.org/10.1524/Ract.2012.2014

Becquerel H (1896) On the rays emitted by phosphorescence. Compt Rend Hebd Seances Acad Sci 122:420–421

Bhuiyan MAH, Bodrud-Doza M, Islam ARMT, Rakib MA, Rahman MS, Ramanathan AL (2016) Assessment of groundwater quality of lakshimpur district of Bangladesh using water quality indices, geostatistical methods, and multivariate analysis. Environ Earth Sci. https://doi.org/10.1007/S12665-016-5823-Y

Bingen B, Demaiffe D, Hertogen J (1996) Redistribution of rare earth elements, thorium, and uranium over accessory minerals in the course of amphibolite to granulite facies metamorphism: the role of apatite and monazite in orthogneisses from Southwestern Norway. Geochim Cosmochim Acta 60:1341–1354. https://doi.org/10.1016/0016-7037(96)00006-3

Birol B, Saridede MN (2013) The effect of reduction parameters on iron Nugget production from composite pellets. Miner Process Extr Metall Rev 34:195–201. https://doi.org/10.1080/08827508.2012.695305

Bonnot F, De Franqueville H, Lourença E (2010) Spatial and spatiotemporal pattern analysis of coconut lethal yellowing in Mozambique. Phytopathology 100:300–312. https://doi.org/10.1094/Phyto-100-4-0300

Bonotto DM (2014) Some features of the Th presence in the Poços De Caldas alkaline Massif, Minas Gerais State, Brazil. In: Thorium: chemical properties, uses and environmental effects. Nova Science Publishers, Inc., pp 109–132

Braun JJ, Pagel M (1994) Geochemical and mineralogical behavior of Ree, Th And U in the akongo lateritic profile (Sw Cameroon). Catena 21:173–177. https://doi.org/10.1016/0341-8162(94)90010-8

Braun JJ et al (2017) Rey-Th–U Solute Dynamics In The Critical Zone: combined Influence Of Chemical Weathering, Atmospheric Deposit Leaching, And Vegetation Cycling (Mule Hole Watershed, South India). Geochem Geophys Geosyst 18:4409–4425. https://doi.org/10.1002/2017gc007158

Buccianti A et al (2009) Natural radioactivity levels (K, Th, U And Rn) in the Cecita Lake Area (Sila Massif, Calabria, Southern Italy): an attempt to discover correlations with soil features on a statistical base. Geoderma 152:145–156. https://doi.org/10.1016/J.Geoderma.2009.05.027

Carr J, Bailey R, Deng E (1985) Use Of Indicator Variograms For An Enhanced Spatial Analysis. Math Geol 17:797–811

Carrasco PC (2010) Nugget Effect, Artificial Or Natural? J Southern Afr Inst Min Metall 110:299–305

Chakrabarti K, Ecka NRR, Mishra B, Babu PVR, Parihar PS (2011) Paleoproterozoic Quartz-Pebble Conglomerate Type Uranium Mineralisation In Mankarhachua Area, Angul District, Orissa. J Geol Soc India 77:443–449. https://doi.org/10.1007/S12594-011-0046-Z

Chan LS, Wong PW, Chen QF (2007) Abundances of radioelements (K, U, Th) in weathered igneous rocks in Hong Kong. J Geophys Eng 4:285–292. https://doi.org/10.1088/1742-2132/4/3/S07

Charro E, Pardo R (2014) Influence of a coal-fired power plant on the thorium levels in soils and on the radioactive hazard for the population. In: Thorium: chemical properties, uses and environmental effects. Nova Science Publishers, Inc., Hauppauge pp 59-89

Chen Q, Gong P (2004) Automatic Variogram Parameter Extraction For Textural Classification Of The Panchromatic Ikonos Imagery. IEEE Trans Geosci Remote Sens 42:1106–1115

Ciuffo LEDC, Belli M (2006) Radioactive Trace In Semi Natural Grassland: Effect Of 40 k In Soil And Potential Remediation. Electron J Biotechnol 9

Clark I (1977a) Practical Kriging in three dimensions. Comput Geosci 3:173–180. https://doi.org/10.1016/0098-3004(77)90038-3

Clark I (1977b) Regularization of a semi-variogram. Comput Geosci 3:341–346

Clark I (1979a) Geostatistics. 2. Semivariogram. 1. Eng Min J 180:90–94

Clark I (1979b) Practical geostatistics, vol 3. Applied Science Publishers, London

Clark I (1979c) Semivariogram—2. Eng Min J 180:92–97

Clark I (2010) Statistics or geostatistics? Sampling error or nugget effect? J Southern Afr Inst Min Metall 110:307–312

Clark I, Eng C (2001) Practical geostatistics

Cowan D, Cooper G (2003) Wavelet analysis of detailed drillhole magnetic susceptibility data, Brockman iron formation, Hamersley Basin, Western Australia. Explor Geophys 34:63–68. https://doi.org/10.1071/Eg03063

Cowart J, Burnett W (1994) The distribution of uranium and thorium decay-series radionuclides in the environment—a review. J Environ Qual 23:651–662

Cressie N (1988) Spatial prediction and ordinary Kriging. Math Geol 20:405–421. https://doi.org/10.1007/Bf00892986

Crossland I (2012) Nuclear fuel cycle science and engineering. Nuclear fuel cycle science and engineering. Elsevier Inc, Amsterdam. https://doi.org/10.1533/9780857096388

Da Costa MAC, De Sousa MZA, Dall'agnol R, Scandolara JE, Ruiz AS (2016) Geochemistry and geochronology of the Rapakivi granites and associated rocks in the midwest portion of the Serra Da Providencia composite Batholith, Sw of Amazonian Craton, Rondonia, Brazil. J S Am Earth Sci 69:194–212. https://doi.org/10.1016/J.Jsames.2016.04.003

Dai Z, Ritzi RW Jr, Dominic DF (2005) Improving permeability semivariograms with transition probability models of hierarchical sedimentary architecture derived from outcrop analog studies. Water Resour Res 41:1–13. https://doi.org/10.1029/2004wr003515

Dauphas N, Pourmand A (2015) Thulium anomalies and rare earth element patterns in meteorites and earth: nebular fractionation and the Nugget effect. Geochim Cosmochim Acta 163:234–261. https://doi.org/10.1016/J.Gca.2015.03.037

David M (2012) Geostatistical ore reserve estimation. Elsevier, Amsterdam

De Assis Silva S, De Souza Lima JS, De Souza GS, De Oliveira RB (2010) Spatial variability of rainfall erosive potential for Espirito Santo State, Brazil. Irriga 15:312–323

Degerlier M, Karahan G, Ozger G (2008) Radioactivity concentrations and dose assessment for soil samples around Adana, Turkey. J Environ Radioact 99:1018–1025

Delbari M, Afrasiab P (2014) Application of indicator and ordinary Kringing for modeling of groundwater chloride. J Environ Stud 40:751–764

Demir Y, Erşahin S, Güler M, Cemek B, Günal H, Arslan H (2009) Spatial variability of depth and salinity of groundwater under irrigated ustifluvents in the Middle Black Sea region of Turkey. Environ Monit Assess 158:279–294. https://doi.org/10.1007/S10661-008-0582-1

Deschamps P, Hillaire-Marcel C, Michelot JL, Doucelance R, Ghaleb B, Buschaert S (2004) U-234/U-238 disequilibrium along stylolitic discontinuities in deep mesozoic limestone formations of the Eastern Paris Basin: evidence for discrete uranium mobility over the last 1-2 million\years. Hydrol Earth Syst Sci 8:35–46. https://doi.org/10.5194/Hess-8-35-2004

Deutsch SJ, Pfeifer PE (1981) Space-time ARMA modeling with contemporaneously correlated innovations. Technometrics 23:401–409

Edahbi M, Plante B, Benzaazoua M, Ward M, Pelletier M (2018) Mobility of rare earth elements in mine drainage: influence of iron oxides, carbonates, and phosphates. Chemosphere 199:647–654. https://doi.org/10.1016/J.Chemosphere.2018.02.054

Engelkemeir D, Flynn K, Glendenin L (1962) Positron emission in the decay of K 40. Phys Rev 126:1818

Ersoy A, Yünsel TY (2018) The assessment of soil contamination by heavy metals using geostatistical sequential gaussian simulation method. Hum Ecol Risk Assess 24:2142–2161. https://doi.org/10.1080/10807039.2018.1440528

Ferronsky VI (2015) Nuclear geophysics: applications in hydrology, hydrogeology, engineering geology, agriculture and environmental science. Nuclear geophysics: applications in hydrology, hydrogeology, engineering geology, agriculture and environmental science. Springer International Publishing, New York. https://doi.org/10.1007/978-3-319-12451-3

Fisher RA (1936) Design of experiments. Br Med J 1:554–554

Frybort J (2014) Comparison of the radiological hazard of thorium and uranium spent fuels from Vver-1000 Reactor. Radiat Phys Chem 104:408–413. https://doi.org/10.1016/J.Radphyschem.2014.05.038

Fu Z, Wang Y, An Z, Hu W, Kmg Mostofa, Li X, Liu B (2018) Spatial and temporal variability of 0- To 5-M soil–water storage at the watershed scale. Hydrol Process 32:2557–2569. https://doi.org/10.1002/Hyp.13172

Gascoyne M, Schwarcz HP, Harmon RS (1982) Carbonate and sulphate precipitates. Oxford University Press, United Kingdom

Genge MJ, Davies B, Suttle MD, Van Ginneken M, Tomkins AG (2017) The mineralogy and petrology of I-type cosmic spherules: implications for their sources, origins and identification in sedimentary rocks. Geochim Cosmochim Acta 218:167–200. https://doi.org/10.1016/J.Gca.2017.09.004

Glikson A (2007) Siderophile element patterns, Pge Nuggets and vapour condensation effects in Ni-rich quench chromite-bearing microkrystite spherules, ~ 3.24 Ga S3 Impact Unit, Barberton Greenstone Belt, Kaapvaal Craton, South Africa. Earth Planet Sci Lett 253:1–16. https://doi.org/10.1016/J.Epsl.2006.10.005

Göl C, Bulut S, Bolat F (2017) Comparison of different interpolation methods for spatial distribution of soil organic carbon and some soil properties in the Black Sea Backward Region of Turkey. J Afr Earth Sci 134:85–91. https://doi.org/10.1016/J.Jafrearsci.2017.06.014

Goovaerts P (2008) Kriging and semivariogram deconvolution in the presence of irregular geographical units. Math Geosci 40:101–128. https://doi.org/10.1007/S11004-007-9129-1

Gundogdu KS, Guney I (2007) Spatial analyses of groundwater levels using Universal Kriging. J Earth Syst Sci 116:49–55. https://doi.org/10.1007/S12040-007-0006-6

Halicz L, Segal I, Fruchter N, Stein M, Lazar B (2008) Strontium stable isotopes fractionate in the soil environments? Earth Planet Sci Lett 272:406–411. https://doi.org/10.1016/J.Epsl.2008.05.005

Hansen RO, Huntington GL (1969) Thorium Movements In Morainal Soils Of The High Sierra, California. Soil Sci 108:257–265

Hansen RO, Stout PR (1968) Isotopic distributions of uranium and thorium in soils. Soil Sci 105:44-50. https://doi.org/10.1097/00010694-196801000-00009

Haug ØT, Galland O, Souloumiac P, Souche A, Guldstrand F, Schmiedel T, Maillot B (2018) Shear versus tensile failure mechanisms induced by sill intrusions: implications for emplacement of conical and saucer-shaped intrusions. J Geophys Res B Solid Earth 123:3430–3449. https://doi.org/10.1002/2017jb015196

Hernandez F, Hernandez-Armas J, Catalan A, Fernandez-Aldecoa JC, Karlsson L (2005) Gross alpha, gross beta activities and gamma emitting radionuclides composition of airborne particulate samples in an oceanic island. Atmos Environ 39:4057–4066. https://doi.org/10.1016/J.Atmosenv.2005.03.035

Hohn ME (1999) Geostatistics and petroleum geology, geostatistics and petroleum geology. Kluwer Academic Publishers, Dordrecht

Horie K, Tsutsumi Y, Cho M, Morishita Y, Hidaka H (2010) Crystallization Of Ree Minerals And Redistribution Of U, Th, and Ree at contact boundary between granite and gabbro during hydrothermal alteration. Phys Chem Earth 35:284–291. https://doi.org/10.1016/J.Pce.2010.03.035

Isaaks E, Srivastava R (1989a) Applied geostatistics. Oxford University Press, New York

Isaaks EH, Srivastava RM (1989b) An introduction to applied geostatistics. Oxford University Press, Oxford

Ivanovich M, Harmon RS (1982) Uranium series disequilibrium: applications to environmental problems. Oxford University Press, Oxford

Ivanovich M, Harmon RS (1992) Uranium-series disequilibrium: applications to earth, marine, and environmental sciences, 2nd edn, 910 p, Clarendon Press, Oxford, ISBN: 019854278X; 978-019854278-0

Jamison R (2014) Thorium: chemical properties, uses and environmental effects. Nova Science Publishers, Inc., Hauppauge, ISBN: 978-163321310-4; 978-163321309-8

Journel A (1986) Geostatistics: models and tools for the earth sciences. Math Geol 18:119–140

Journel AG, Huijbregts CJ (1978) Mining geostatistics. Academic Press, New York

Kacmaz H, Burns PC (2017) Uranyl phosphates and associated minerals in the Koprubasi (Manisa) uranium deposit, Turkey. Ore Geol Rev 84:102–115. https://doi.org/10.1016/J.Oregeorev.2017.01.001

Karacan CÖ (2012) Geostatistical assessment and quantification of uncertainty of methane in the caved and fractured zone of longwall mines. In: Proceedings of the SME annual meeting and exhibit, pp 24–31. ISBN: 978-162276089-3

Kaufman A (2005) U and Th series nuclides in natural waters. In: Isotopes in the water cycle: past, present and future of a developing science. Springer, Amsterdam, pp 97–107. https://doi.org/10.1007/1-4020-3023-1_8

Kavurmaci M (2016) Evaluation of groundwater quality using a Gis-Mcda-based model: a case study in Aksaray. Environ Earth Sci, Turkey. https://doi.org/10.1007/S12665-016-6074-7

Kenny GG et al (2019) A New U-Pb age for shock-recrystallised zircon from the lappajarvi impact crater, Finland, and implications for the accurate dating of impact events. Geochim Cosmochim Acta 245:479–494. https://doi.org/10.1016/J.Gca.2018.11.021

Khosravi Y, Zamani AA, Parizanganeh AH, Yaftian MR (2018) Assessment of spatial distribution pattern of heavy metals surrounding a lead and zinc production plant in Zanjan Province, Iran. Geoderma Reg 12:10–17. https://doi.org/10.1016/J.Geodrs.2017.12.002

Kiss J, De Jong E, Bettany J (1988) The distribution of natural radionuclides in native soils of Southern Saskatchewan, Canada. J Environ Qual 17:437–445

Külahcı F (2005) Determination of the natural radioactivity of the Keban Dam Lake Uluova section. Unpublished PhD Thesis, Institute of Natural and Applied Sciences, Phyiscs Department, Nuclear Physics Division, Fırat University, Elazığ, Harput, Turkiye

Külahcı F (2016a) Proposals for risk assessment of major cations in surface water and deep sediment: iso-cation curves, probabilities of occurrence and non-occurrence of cations. Environ Earth Sci. https://doi.org/10.1007/S12665-016-5788-X

Külahcı F (2016b) Spatiotemporal (four-dimensional) modeling and simulation of uranium (238) in Hazar Lake (Turkey). Water Environ Earth Sci. https://doi.org/10.1007/S12665-016-5302-5

Kulahci F, Sen Z (2014) On the correction of spatial and statistical uncertainties in systematic measurements of Rn-222 for earthquake prediction. Surv Geophys 35:449–478. https://doi.org/10.1007/S10712-013-9273-8

Külahcı F, Şen Z (2007) Spatial dispersion modeling of 90 Sr by point cumulative semivariogram at Keban Dam Lake, Turkey. Appl Radiat Isot 65:1070–1077

Külahcı F, Şen Z (2009a) Potential utilization of the absolute point cumulative semivariogram technique for the evaluation of distribution coefficient. J Hazard Mater 168:1387–1396. https://doi.org/10.1016/J.Jhazmat.2009.03.027

Külahcı F, Şen Z (2009b) Spatio-temporal modeling of Pb-210 transportation in Lake. Environ J Hazard Mater 165:525–532. https://doi.org/10.1016/J.Jhazmat.2008.10.026

Külahcı F, Şen Z, Kazanç S (2008) Cesium concentration spatial distribution modeling by point cumulative semivariogram. Water Air Soil Pollut 195:151

L'annunziata MF (2003) Handbook of radioactivity analysis, handbook of radioactivity analysis. Elsevier Inc, Amsterdam. https://doi.org/10.1016/b978-0-12-436603-9.x5000-5

Latta DE, Kemner KM, Mishra B, Boyanov MI (2016) Effects of calcium and phosphate on uranium(Iv) oxidation: comparison between nanoparticulate uraninite and amorphous U-Iv-phosphate. Geochim Cosmochim Acta 174:122–142. https://doi.org/10.1016/J.Gca.2015.11.010

Laubenstein M, Magaldi D (2008) Natural radioactivity of some red mediterranean soils. CATENA 76:22–26. https://doi.org/10.1016/J.Catena.2008.08.005

Leptoukh G, Zubko V, Gopalan A (2007) Spatial aspects of multi-sensor data fusion: aerosol optical thickness, pp 3119–3122. https://doi.org/10.1109/igarss.2007.4423505

Li HJ, Kegler P, Klepov VV, Klinkenberg M, Bosbach D, Alekseev EV (2018a) Comparison of uranium(Vi) and thorium(Iv) silicates synthesized via mixed fluxes techniques. Inorg Chem 57:6734–6745. https://doi.org/10.1021/Acs.Inorgchem.8b01072

Li Z, Zhang X, Clarke KC, Liu G, Zhu R (2018b) An automatic variogram modeling method with high reliability fitness and estimates. Comput Geosci 120:48–59. https://doi.org/10.1016/J.Cageo.2018.07.011

Li ZZ, Hadioui M, Wilkinson KJ (2019) Conditions affecting the release of thorium and uranium from the tailings of a niobium mine. Environ Pollut 247:206–215. https://doi.org/10.1016/J.Envpol.2018.12.042

Liu X, Xia J, Blenkinsopp C, Arnold L, Wright G (2014) High water mark determination based on the principle of spatial continuity of the swash probability. J Coast Res 30:487–499. https://doi.org/10.2112/Jcoastres-D-12-00061.1

Lü C, Zhang X, Liu G, Wu J, Yan H, Deng C (2012) Characteristics of seed rain of haloxylon ammodendron in southeastern edge of Junggar Basin Shengtai Xuebao. Acta Ecol Sin 32:6270–6278. https://doi.org/10.5846/Stxb201107161059

Lütkepohl H, Krätzig M (2004) Applied time series econometrics. Cambridge University Press, Cambridge

Ma YZ, Jones TA (2001) Modeling hole-effect variograms of lithology-indicator variables. Math Geol 33:631–648. https://doi.org/10.1023/A:1011001029880

Ma H, Li D, Jin S, Zhang X (2001) Image comparison based on semivariogram and its application. In: Bhanu B, Shen J, Zhang T (eds) Proceedings of SPIE - The International Society for Optical Engineering, conference paper, 4552, 140–147

Masod Abdulqader S, Vakanjac B, Kovacevic J, Naunovic Z, Zdjelarevic N (2018) Natural radioactivity of intrusive-meta-morphic and sedimentary rocks of the Balkan mountain range (Serbia. Minerals, Stara Planina). https://doi.org/10.3390/Min8010006

Matheron G (1963) Principles of geostatistics. Econ Geol 58:1246–1266. https://doi.org/10.2113/Gsecongeo.58.8.1246

Matheron G (1970) Random structures and mathematical geology. Rev Int Stat Inst 38:1

Meddaugh WS (2006) Reservoir modeling for mature fields—impact of workflow and up-scaling on fluid flow response. In: Society of petroleum engineers, 68th European association of geoscientists and engineers conference and exhibition, incorporating SPE EUROPEC 2006, EAGE 2006: opportunities in mature areas, 2, pp 699–716

Meinhold G (2010) Rutile and its applications in earth sciences. Earth Sci Rev 102:1–28. https://doi.org/10.1016/J.Earscirev.2010.06.001

Mesbah A, Clavier N, Lozano-Rodriguez MJ, Szenknect S, Dacheux N (2016) Incorporation of thorium in the zircon structure type through the Th1-Xerx(Sio4)(1-X)(Po4)(X) thorite-xenotime solid solution. Inorg Chem 55:11273–11282. https://doi.org/10.1021/Acs.Inorgchem.6b01862

Middleton MF, Brett J, Flint D (2014) Thorium occurrence: geological and geophysical implications for Western Australia. Thorium: chemical properties, uses and environmental effects. Nova Science Publishers Inc, Hauppauge, pp 133–178

Mirás-Avalos JM, Mestas-Valero RM, Sande-Fouz P, Paz-González A (2009) Consistency analysis of pluviometric information in Galicia (Nw Spain). Atmos Res 94:629–640. https://doi.org/10.1016/J.Atmosres.2009.05.011

Morales-Arredondo JI, Hernandez MAA, Hernandez-Mendiola E, Estrada-Hernandez RE, Om Bermea (2018) Hydrogeochemical behavior of uranium and thorium in rock and groundwater samples from southeastern of El Bajio Guanajuatese. Environmental Earth Sciences, Guanajuato. https://doi.org/10.1007/S12665-018-7749-Z

Nair RN, Sunny F, Chopra M, Sharma LK, Puranik VD, Ghosh AK (2014) Estimation of radioactive leakages into the Pacific Ocean due to Fukushima nuclear accident. Environ Earth Sci 71:1007–1019. https://doi.org/10.1007/S12665-013-2501-1

Ndjigui PD, Bilong P, Bitom D, Dia A (2008) Mobilization and redistribution of major and trace elements in two weathering profiles developed on serpentinites in the Lomie Ultramafic Complex, South-East Cameroon. J Afr Earth Sci 50:305–328. https://doi.org/10.1016/J.Jafrearsci.2007.10.006

Niksarlıoğlu S, Külahcı F, Şen Z (2015) Spatiotemporal modeling and simulation of chernobyl radioactive fallout in Northern Turkey. J Radioanal Nucl Chem 303:171–186. https://doi.org/10.1007/S10967-014-3517-Z

Nirala M (2008) Multi-sensor data fusion of aerosol optical thickness. Int J Remote Sens 29:2127–2136. https://doi.org/10.1080/01431160701395336

Not C, Brown K, Ghaleb B, Hillaire-Marcel C (2012) Conservative behavior of uranium vs. salinity in Arctic Sea Ice and Brine. Mar Chem 130:33–39. https://doi.org/10.1016/J.Marchem.2011.12.005

Nwankpa AC (2017) Determination of food crops contamination in Osun State, Nigeria due to radium-226, thorium-232 and potassium-40 concentrations in the environment. Eur J Sustain Dev 6:169–174

Ojovan MI, Lee WE, Lee W (2005) An introduction to nuclear waste immobilisation. An introduction to nuclear waste immobilisation. Elsevier Ltd, Amsterdam. https://doi.org/10.1016/b978-0-08-044462-8.x5000-5

Oldham L et al (2017) Red Nuggets grow inside-out: evidence from gravitational lensing. Mon Not R Astron Soc 465:3185–3202. https://doi.org/10.1093/Mnras/Stw2832

Olea RA (2007) Declustering of clustered preferential sampling for histogram and semivariogram inference. Math Geol 39:453–467. https://doi.org/10.1007/S11004-007-9108-6

Oropeza JAP, Vélez EP, Vélez OP (2018) Adjustment of a spherical variogram of the annual precipitation of the climatological normals 1951–2010. Tecnol Y Ciencias Del Agua 9:209–222. https://doi.org/10.24850/j-tyca-2018-06-10

Oyedele J, Shimboyo S, Sitoka S, Gaoseb F (2010) Assessment of natural radioactivity in the soils of Rössing uranium mine and its satellite town in western Namibia, Southern Africa. Nuclear Instrum Methods Phys Res Sect A Accel Spectrom Detect Assoc Equip 619:467–469

Öztopal A (2006) Artificial neural network approach to spatial estimation of wind velocity data. Energy Convers Manage 47:395–406. https://doi.org/10.1016/J.Enconman.2005.05.009

Özyavuz M, Cemil Bilgili B, Elkiran G (2015) Temperature distribution and environmental impact of Tekirdag Ataturk Forest Nature Park. Int J Global Warm 8:102–113. https://doi.org/10.1504/Ijgw.2015.071581

Papastefanou C (2010) Escaping radioactivity from coal-fired power plants (CPPS) due to coal burning and the associated hazards: a review. J Environ Radioact 101:191–200

Pardo-Igúzquiza E, Dowd PA (2004) Normality tests for spatially correlated data. Math Geol 36:659–682. https://doi.org/10.1023/B:Matg.0000039540.43774.2b

Petrus JA, Kenny GG, Ayer JA, Lightfoot PC, Kamber BS (2016) Uranium-lead zircon systematics in the sudbury impact Crater-Fill: implications for target lithologies and crater evolution. J Geol Soc 173:59–75. https://doi.org/10.1144/Jgs2014-056

Pingguo Y, Byrne JM, Yang M (2016) Spatial variability of soil magnetic susceptibility, organic carbon and total nitrogen from farmland in Northern China. Catena 145:92–98. https://doi.org/10.1016/J.Catena.2016.05.025

Rabbel O, Galland O, Mair K, Lecomte I, Senger K, Spacapan JB, Manceda R (2018) From field analogues to realistic seismic modelling: a case study of an oil-producing andesitic sill complex in the Neuquén Basin, Argentina. J Geol Soc 175:580–593. https://doi.org/10.1144/Jgs2017-116

Rehman HU et al (2013) Ion microprobe U–Th–Pb geochronology and study of micro-inclusions in zircon from the Himalayan High- and ultrahigh-pressure Eclogites, Kaghan Valley of Pakistan. J Asian Earth Sci 63:179–196. https://doi.org/10.1016/J.Jseaes.2012.04.025

Rodriguez PB, Tome FV, Lozano JC (2017) Influence of soil structure on the "F-V Approach" applied to U-238 and Ra-226. Chemosphere 168:832–838. https://doi.org/10.1016/J.Chemosphere.2016.10.127

Rogers J, Adams J, Wedepohl K (1969) Handbook of geochemistry. Springer, Berlin **(Ii/3, Sections 90)**

Rosemary F, Vitharana UWA, Indraratne SP, Weerasooriya R, Mishra U (2017) Exploring the spatial variability of soil properties in an Alfisol soil Catena. Catena 150:53–61. https://doi.org/10.1016/J.Catena.2016.10.017

Saghafian B, Bondarabadi SR (2008) Validity of regional rainfall spatial distribution methods in mountainous areas. J Hydrol Eng 13:531–540. https://doi.org/10.1061/(Asce)1084-0699(2008)13:7(531)

Şahin A, Şen Z (2004) A new spatial prediction model and its application to wind records. Theor Appl Climatol 79:45–54. https://doi.org/10.1007/S00704-004-0037-8

Saleh H, Abu Shayeb M (2014) Natural radioactivity distribution of southern part of Jordan (Ma'an) soil. Ann Nuclear Energy 65:184–189. https://doi.org/10.1016/J.Anucene.2013.10.042

Samat SB, Green S, Beddoe AH (1997) The activity of one gram of potassium. Phys Med Biol 42:407

Scott M (1982) The chemistry of U And Th series nuclides in rivers. In: Uranium series disequilibrium: applications to environmental problems

Şen Z (1989) Cumulative semivariogram models of regionalized variables. Math Geol 21:891–903. https://doi.org/10.1007/Bf00894454

Şen Z (1997) Objective analysis by cumulative semivariogram technique and its application in Turkey. J Appl Meteorol 36:1712–1724

Şen Z (1998a) An application of a regional air pollution estimation model over Istanbul urban area. Atmos Environ 32:3425–3433. https://doi.org/10.1016/S1352-2310(98)00040-5

Şen Z (1998b) Point cumulative semivariogram for identification of heterogeneities in regional seismicity of Turkey. Math Geol 30:767–787. https://doi.org/10.1023/A:1021704507596

Şen Z (2009) Spatial modeling principles in earth sciences. Springer, New York

Şen Z, Şahin AD (1998) Regional wind energy evaluation in some parts of Turkey. J Wind Eng Ind Aerodyn 74:345–353

Şen Z, Şahin AD (2001) Spatial interpolation and estimation of solar irradiation by cumulative semivariograms. Sol Energy 71:11–21

Şengün M (2008) Relations between land use and geomorphological units in Uluova. In: National geomorphology symposium. (Uluova'da jeomorfolojik birimlerle arazi kullanımı arasındaki ilişkiler Ulusal Jeomorfoloji Sempozyumu), pp 20–23

Serre NBC, Alban C, Bourguignon J, Ravanel S (2019) Uncovering the physiological and cellular effects of uranium on the root system of *Arabidopsis Thaliana*. Environ Exp Bot 157:121–130. https://doi.org/10.1016/J.Envexpbot.2018.10.004

Sheppard MI (1980) The environmental behaviour of uranium and thorium. Atomic Energy of Canada Ltd. (Report Aecl–6795)

Shmelev AN, Kulikov GG, Kulikov EG, Apse VA, Geraskin NI (2014) Unique role of thorium in closed (Th–U–Pu)-fuel cycle due to the involvement of hybrid "Fusion-Fission" reactors with Th-blanket to generate advanced (231pa + 232u + 233u)-fuel: long-life power reactor cores and non-proliferation. Thorium: chemical properties, uses and environmental effects. Nova Science Publishers Inc, Hauppauge, pp 211–239

Shurtz RF (1983) Mathematics of mine sampling VII: the contradictory spherical Semivariogram model. Trans Am Inst Min Metall Pet Eng Soc Min Eng 274:1931–1933

Some'e BS, Hassanpour F, Ezani A, Miremadi SR, Tabari H (2011) Investigation of spatial variability and pattern analysis of soil properties in the northwest of Iran. Environ Earth Sci 64:1849–1864. https://doi.org/10.1007/S12665-011-0993-0

Student (1907) On the error of counting with a haemacytometer. Biometrika 351–360

Suhana J, Rashid M (2016) Naturally occurring radionuclides in particulate emission from a coal fired power plant: a potential contamination? J Environ Chem Eng 4:4904–4910

Talibudeen O, Beasley J, Lane P, Rajendran N (1978) Assessment of soil potassium reserves available to plant roots. J Soil Sci 29:207–218

Tarawneh QY (2015) Spatial variation of Saudi Arabia's annual rainfall using a regional prediction model. Arab J Geosci 8:4147–4160. https://doi.org/10.1007/S12517-014-1468-X

Tarawneh Q, Şen Z (2012) Spatial climate variation pattern and regional prediction of rainfall in Jordan. Water Environ J 26:252–260. https://doi.org/10.1111/J.1747-6593.2011.00284.X

Tricca A, Wasserburg GJ, Porcelli D, Baskaran M (2001) The transport of U- and Th-series nuclides in a sandy unconfined aquifer. Geochim Cosmochim Acta 65:1187–1210. https://doi.org/10.1016/S0016-7037(00)00617-7

Tudorache A, Marin C (2012) Assessing the heavy metal content of suspended particulate matter and of groundwater occurring in the area of the future weak- and -medium radioactive waste repository saligny, Romania. Carpath J Earth Env 7:165–172

Valeriano MM, Kuplich TM, Storino M, Amaral BD, Mendes JN Jr, Lima DJ (2006) Modeling small watersheds in Brazilian Amazonia with shuttle radar topographic mission-90 M data. Comput Geosci 32:1169–1181. https://doi.org/10.1016/J.Cageo.2005.10.019

Valkovic V (2000) Radioactivity in the environment: physicochemical aspects and applications. Elsevier, Amsterdam

Van Der Loeff MMR, Moore WS (2007) Determination of natural radioactive tracers. In: Methods of seawater analysis: third, completely revised and extended edition. Wiley Blackwell, New York, pp 365–397. https://doi.org/10.1002/9783527613984.ch13

Vandyk TM et al (2018) Precambrian olistoliths masquerading as sills from Death Valley, California. J Geol Soc 175:377–395. https://doi.org/10.1144/Jgs2017-002

Varouchakis EA, Kolosionis K, Karatzas GP (2016) Spatial variability estimation and risk assessment of the aquifer level at sparsely gauged basins using geostatistical methodologies. Earth Sci Inf 9:437–448. https://doi.org/10.1007/S12145-016-0265-3

Vázquez EV, Vieira SR, De Maria IC, González AP (2009) Geostatistical analysis of microrelief of an oxisol as a function of tillage and cumulative rainfall. Sci Agricola 66:225–232

Vázquez EV, Bertol I, Siqueira GM, Paz-Ferreiro J, Dafonte Dafonte J (2010a) Evolution of the soil surface roughness using geostatistical analysis. Bragantia 69:141–152. https://doi.org/10.1590/S0006-87052010000500015

Vázquez EV, Vieira SR, De Maria IC, González AP (2010b) Fractal dimension and geostatistical parameters for soil microrelief as a function of cumulative precipitation. Sci Agricola 67:78–83

Velasco-Forero CA, Sempere-Torres D, Cassiraga EF, Jaime Gómez-Hernández J (2009) A non-parametric automatic blending methodology to estimate rainfall fields from rain gauge and radar data. Adv Water Resour 32:986–1002. https://doi.org/10.1016/J.Advwatres.2008.10.004

Verma MB, Roy MK, Saxena V (2003) Uranium and polymetallic sulphide mineralisation in the banded iron formation at Udaisagar, Udaipur District, Rajasthan. J Geol Soc India 61:703–710

Verworn A, Haberlandt U (2011) Spatial interpolation of hourly rainfall-effect of additional information, variogram inference and storm properties. Hydrol Earth Syst Sci 15:569–584. https://doi.org/10.5194/Hess-15-569-2011

Vidal Vázquez E, Vivas Miranda JG, Paz González A (2005) Characterizing anisotropy and heterogeneity of soil surface microtopography using fractal models. Ecol Model 182:337–353. https://doi.org/10.1016/J.Ecolmodel.2004.04.012

Vidal Vázquez E, Miranda JGV, González AP (2007) Describing soil surface microrelief by crossover length and fractal dimension. Nonlinear Process Geophys 14:223–235. https://doi.org/10.5194/Npg-14-223-2007

Vigier N et al (2005) Mobility of U-series nuclides during basalt weathering: an example from the Deccan Traps (India). Chem Geol 219:69–91. https://doi.org/10.1016/J.Chemgeo.2005.02.010

War SA, Nongkynrih P, Khathing DT, Iongwai PS, Dkhar LM (2012) Assessment of the radiological hazards of sand sediments collected from streams and streamlets of the uranium deposit areas in West Khasi Hills District, Meghalaya, India. Environ Earth Sci 65:1695–1703. https://doi.org/10.1007/S12665-011-1147-0

Watford GA, Wethington JA (1981) Radiological hazards of uranium mill tailings piles. Nucl Technol 53:295–302. https://doi.org/10.13182/nt81-a32640

WHO (2018) WHO. http://Apps.Who.Int/Iris/Handle/10665/66930. Accessed 31 Jul 2018

World Nuclear Association (2013) World Nuclear Association. http://www.World-Nuclear.org/Information-Library/Current-And-Future-Generation/Thorium.Aspx. Accessed 12 Apr 2013

Wu T, Xiao L, Wilde SA, Ma CQ, Li ZL, Sun Y, Zhan QY (2016) Zircon U–Pb Age And Sr–Nd–Hf isotope geochemistry of the Ganluogou Dioritic complex in the northern Triassic Yidun arc belt, eastern Tibetan Plateau: implications for the closure of the Garze-Litang ocean. Lithos 248:94–108. https://doi.org/10.1016/J.Lithos.2015.12.029

Xu SP, Tao S, Xu FL, Cao J (2000) Spatial distribution pattern of trace elements contents in the soil in inner Mongolia. Acta Geogr Sin 55:337–345

Yalcin MG, Ilhan S (2013) Major and trace element geochemistry of bauxites of Ayranci, Karaman, Central Bolkardag, Turkey. Asian J Chem 25:2893–2904. https://doi.org/10.14233/ajchem.2013.14275

Yamamoto JK, Chao L (2009) Comparison of methods for bigaussianity tests. Geociencias 28:121–128

Yao Z, He G, Li CF, Dong C (2018) Sill geometry and emplacement controlled by a major disconformity in the Tarim Basin, China. Earth Planet Sci Lett 501:37–45. https://doi.org/10.1016/J.Epsl.2018.08.026

Yates F (1939) The comparative advantages of systematic and randomized arrangements in the design of agricultural and biological experiments. Biometrika 30:440–466

Zakirov ES, Indrupskiy IM, Liubimova OV, Shiriaev IM, Anikeev DP (2017) Geostatistically consistent history matching of 3d oil-and-gas reservoir models. Dokl Earth Sci 476:1120–1124. https://doi.org/10.1134/s1028334x17100117

Zas R, Solla A, Sampedro L (2007) Variography and Kriging allow screening pinus pinaster resistant to Armillaria Ostoyae in field conditions. Forestry 80:201–209. https://doi.org/10.1093/Forestry/Cpl050

Zelenika KN, Malvić T (2010) Sequential indicator simulations of sandstone reservoir thickness. In: Sava depression, Croatia (Sw Part Of Pannonian Basin), IAMG 2010 Budapest—14th annual conference of the international association for mathematical geosciences

Zhang CS, Fay D, Mcgrath D, Grennan E, Carton OT (2008) Use of trans-Gaussian Kriging for national soil geochemical mapping in Ireland. Geochem Explor Environ Anal 8:255–265. https://doi.org/10.1144/1467-7873/08-173

Zhang P, Zhang J, Wang J, Li M, Liang J, Wu Y (2018) Flow units classification for geostatisitical three-dimensional modeling of a non-marine sandstone reservoir: a case study from the Paleocene Funing Formation of the Gaoji Oilfield, East China. Open Geosci 10:113–120. https://doi.org/10.1515/Geo-2018-0009

Zhao J, Li F, Fu H, Tian Y, Hu Z (2007) A DEM-based partition adjustment for the interpolation of annual cumulative temperature in China. https://doi.org/10.1117/12.763506

Publisher's Note Springer Nature remains neutral with regard to jurisdictional claims in published maps and institutional affiliations.